Numerical investigation of neutral atmospheric boundary layer flows over flat terrain and three-dimensional hills considering the effects of Coriolis force

Tong Zhou , Takeshi Ishihara [*]

Department of Civil Engineering, School of Engineering, The University of Tokyo, 113-8656, Japan

ARTICLE INFO

ABSTRACT

The characteristics of neutral atmospheric boundary layer (ABL) flows can be strongly affected by terrain and earth rotation-induced Coriolis force. The purpose of this study is to ascertain the effects of Coriolis force on neutral ABL flows over flat terrain and isolated three-dimensional hills. Based on large-eddy simulations (LES), a new formula for the maximum turbulence length scale l_{max} in the limited-length-scale (LLS) k-ε model is proposed to reproduce neutral ABL flows over flat terrain with different exposure conditions. It is demonstrated that l_{max} can be reasonably expressed as a function of the geostrophic wind speed U_g, the Coriolis parameter f_c and the roughness length z_0. The effects of Coriolis force on atmospheric flows over single isolated hills are subsequently elucidated from the perspective of flow patterns and turbulent statistics. The wake trajectory deflection and asymmetric vortex structures are identified on the lee side of hills owing to the wind veer. Additionally, lateral wind shear associated with the Coriolis force contributes to a faster wake recovery and larger turbulence fluctuations downstream of steep hills. Moreover, the speed-up factor at the hilltop is significantly enhanced with increasing hill slopes and height ratios, while it is not sensitive to the Coriolis effects.

1. Introduction

In recent years, the ever-growing demand for clean and renewable energy has led to a massive increase in large wind power plants operating in complex terrain. The accurate prediction of atmospheric boundary layer (ABL) flows over mountainous terrain is crucial for the effective utilization of wind resources in hilly areas. Based on the similarity law theory, many wind tunnel experiments have been carried out to advance the knowledge of complicated interactions between the unidirectional ABL flows and curved topography (Ishihara et al., 1999, 2001; Takahashi et al., 2005; Cao and Tamura, 2006, 2007; Conan et al., 2016; Li et al., 2017; Kamada et al., 2019). With the rapid improvement of numerical methodologies and the tremendous growth of computational resources, computational fluid dynamics (CFD) simulation has become another indispensable method to evaluate the potential of wind energy resource and the feasibility of wind power utilization in hilly regions. Based on the assumption of unidirectional incoming wind conditions, extensive CFD-assisted studies have been carried out to shed light on the effects of topographical factors on neutral ABL flows over curved topography, with focus on the hill slope (Ferreira et al., 1995;

Kim et al., 1997; Tamura et al., 2007a, 2007b; Liu et al., 2020; Yang et al., 2021), hill shape (Ishihara and Hibi, 2002; Liu et al., 2016a; Pirooz and Flay, 2018; Ishihara and Qi, 2019; Zhou et al., 2022) and surface roughness (Brown et al., 2001; Cao et al., 2012; Liu et al., 2016b, 2019). Nevertheless, idealized unidirectional inflow boundary conditions cannot reflect the wind veer attributed to Coriolis effects, thus deviating from actual ABL flows. The wind veering phenomenon within the ABL has been extensively validated and investigated by numerous observational studies (Lettau, 1950; Mendenhall, 1967; Yeo and Simiu, 2010; He et al., 2013, 2016; Shu et al., 2018, 2020). As a consequence of the Coriolis force, the wind direction varied with height throughout the entire ABL. To quantitatively analyze wind veer effects, the mean veering angle is widely used in previous research (Tse et al., 2016; Liu et al., 2019), which is defined as the difference between the mean wind direction at the ground surface and at a height of interest. In practice, the mean wind veering angle is comprehensively influenced by a range of geographical and environmental factors (Kelly and van der Laan, 2023), such as the topographic conditions (Yeo, 2012; Weerasuriya et al., 2016; Shu et al., 2018, 2020), thermal stratification (Mendenhall, 1967; Brown et al., 2005; Peña et al., 2014), and diurnal cycles (Crawford and Hudson, 1973). However, the effects of Coriolis force on

---

Nomenclature

f_c	Coriolis parameter [s^{-1}]
Gr_1, Gr_2	growth ratio of grid spacing (streamwise, vertical) [-]
h	height of the three-dimensional hill [m]
H	height of the atmospheric boundary layer [m]
l_m	turbulence length scale [m]
l_{max}	maximum turbulence length scale [m]
L	half-width of the three-dimensional hill [m]
L_x, L_y, L_z	computational domain size of the numerical model (streamwise, spanwise and vertical) [m]
N_x, N_y, N_z	grid number of the numerical model (streamwise, spanwise and vertical) [-]
Ro_h	effective Rossby number defined by the hill height [-]
Ro_s	surface Rossby number defined by the surface roughness length [-]
T	sampling period [s]
$U(z')$	mean wind speed at the relative height above the local terrain ($z' = z - z_s$) [m s^{-1}]
$U_0(z')$	reference mean wind speed at the relative height z' in the absence of the hill [m s^{-1}]
U_g	gradient wind speed [m s^{-1}]
U_{ref}	freestream velocity in the wind tunnel experiment [m s^{-1}]
z_0	surface roughness length [m]
z_g	gradient height [m]
z_g^*	normalized gradient height [-]
θ_s	hill slope [-]
ΔS	speed-up factor [-]
Δt	time step size [s]
$\Delta x, \Delta y, \Delta z$	grid spacing of the numerical model (streamwise, spanwise and vertical) [m]

atmospheric flows over hills have rarely been considered in existing literature except for a few research works (Peng et al., 1995; Petersen et al., 2005; Liu and Stevens, 2021), which may lead to uncertainty regarding the wind resource assessment in mountainous regions.

To recreate the wind veering phenomenon induced by the Coriolis force throughout the whole ABL in the boundary layer wind tunnel, some researchers have designed pioneering apparatuses such as the artificial rotational system (Caldwell et al., 1972; Howroyd and Slawson, 1975) and the vane-based system (Flay, 1996; Tse et al., 2016; Weerasuriya et al., 2018; Liu et al., 2019). Nevertheless, it is noteworthy that these experimental devices may encounter challenges in replicating target wind profiles that fulfill all desired characteristics of mean wind and turbulence in ABL flow fields. Over the years, CFD-based numerical techniques have been developed to gain a better understanding of Coriolis effects on atmospheric flows. Since direct numerical simulation (DNS) is computationally impractical for high-Reynolds-number ABL flows, large eddy simulation (LES) and Reynolds-averaged Navier--Stokes (RANS) turbulence models are more promising for the modeling of atmospheric flows considering the Coriolis effects. Several LES studies have been performed to clarify the influence of Coriolis force on ABL structures (Kosović and Curry, 2000; Esau, 2003, 2004; Pedersen et al., 2014; Jiang et al., 2018; Lu and Li, 2022). With regards to RANS simulations, the limited-length-scale (LLS) turbulence closures have been developed by Blackadar (1962) and Apsley and Casrto (1997) to reproduce mean wind profiles in the ABL considering the effects of Coriolis force. In which, the difficulty that single-length-scale RANS models (e.g., mixing-length model, standard k-ε model) have for recognizing the finite ABL depth are addressed. The maximum turbulence length scale l_{max} is introduced as the length scale limiter to account for the ABL depth, which was roughly estimated to be $l_{max} = 0.00027U_g/f_c$ by Blackadar (1962) for neutral ABL flows over flat terrain. However, this formula cannot reasonably reflect the effects of terrain roughness on mean wind profiles in neutral ABL flow fields. As clearly demonstrated by Meng et al. (1995), the gradient height z_g of neutral ABL flows is not only a function of the length scale U_g/f_c but also the surface Rossby number $Ro_s (= U_g/f_c z_0)$. Moreover, it is also well evidenced by previous studies (Hess and Garratt, 2002b; Lindvall and Svensson, 2019) that the mean wind direction is strongly dependent on the surface Rossby number, in which the mean wind veering angle increases with the terrain roughness. Therefore, the formula for estimating l_{max} needs to be modified to account for the effects of different surface roughness on neutral ABL flows.

In this study, the performance of the LLS k-ε model in simulating atmospheric flows over flat terrain and three-dimensional hills is first examined. Based on LES simulations, a new formula for l_{max} is then proposed to reproduce neutral ABL flows over flat terrain with different

surface roughness considering the effects of Coriolis force. Finally, by using the LLS k-ε model, the characteristics of atmospheric flows over three-dimensional hills with different hill slopes and height ratios (hill height/ABL height) are investigated. The impacts of Coriolis force on mean flow patterns and turbulent flow characteristics over hills are clarified.

This paper is structured as follows: Section 2 details the numerical methodology employed in this study, including the governing equations and the turbulence models. The validity of the numerical models in predicting atmospheric flows over flat terrain and three-dimensional hills is verified in Section 3. Section 4 derives a new formula for l_{max} to reproduce neutral ABL flows over flat terrain with different surface roughness by the LLS k-ε model. The effects of the Coriolis force on atmospheric flows over three-dimensional hills are elucidated in Section 5. Finally, Section 6 briefly outlines the new findings of the present study.

2. Numerical methodology

The governing equations for RANS and LES simulations adopted in this study are presented in Section 2.1. And the subsequent two sections (Section 2.2 and Section 2.3) introduce the turbulence closures for the LLS k-ε model and the LES model, respectively.

2.1. Governing equations

In regard to the RANS and LES modelling, the continuity and momentum equations for neutral ABL flows can be expressed as follows:

$$\frac{\partial \rho \overline{u}_i}{\partial x_i} = 0 \tag{1}$$

$$\frac{\partial \rho \overline{u}_i}{\partial t} + \frac{\partial}{\partial x_j}\left(\rho \overline{u}_i \overline{u}_j\right) = -\frac{\partial \overline{p}}{\partial x_i} + \frac{\partial}{\partial x_j}\left[\mu\left(\frac{\partial \overline{u}_i}{\partial x_j} + \frac{\partial \overline{u}_j}{\partial x_i}\right)\right] + \rho f_c \varepsilon_{ij3}\left(G_j - \overline{u}_j\right) - \frac{\partial \tau_{ij}}{\partial x_j} \tag{2}$$

where the overbar signifies the space filtering operation for LES and the time-averaged operation for RANS, respectively; u_i and u_j are the velocity components; p is the pressure; ρ is the air density; μ is the molecular viscosity; f_c is the Coriolis parameter; ε_{ij3} is the altering unit tensor; G_j is the geostrophic wind speed component. τ_{ij} is introduced to account for the differences between $\overline{u_i u_j}$ and $\overline{u}_i \overline{u}_j$:

$$\tau_{ij} = -\rho\left(\overline{u_i u_j} - \overline{u}_i \overline{u}_j\right) = -\rho \overline{u_i' u_j'} \tag{3}$$

τ_{ij} is termed as the time-averaged Reynolds stress in RANS models, which represents the influence of turbulent vortices on the mean flow field. By contrast, τ_{ij} is known as the SGS Reynolds stress in LES models, which stands for the effect of unresolved small-scale fluid motions on

resolved large-scale fluid motions. For the closure of the governing equations, τ_{ij} needs to be modeled.

Moreover, it should be noted that only the horizontal components of the Coriolis force are considered in this study. The vertical component of the Coriolis force is much smaller than the gravitational force, and thus it is generally assumed to be negligible in wind engineering and wind energy communities (Koblitz et al., 2015; Feng et al., 2019; Gadde and Stevens, 2019; Lu and Li, 2022; Liu and Stevens, 2022; Qian et al., 2022).

2.2. LLS k-ε model

In the LLS k-ε model, the time-averaged Reynolds stress τ_{ij} is characterized by using the linear eddy viscosity model:

$$\tau_{ij} = -\rho \overline{u_i' u_j'} = 2\mu_t \overline{S}_{ij} - \frac{2}{3}\rho k \delta_{ij} \tag{4}$$

$$\overline{S}_{ij} = \frac{1}{2}\left(\frac{\partial \overline{u}_i}{\partial x_j} + \frac{\partial \overline{u}_j}{\partial x_i}\right) \tag{5}$$

where $\overline{S}_{ij}$ is the strain-rate tensor, δ_{ij} is the Kronecker delta and the isotropic part of the stress tensor ($2/3\rho k \delta_{ij}$) is implicitly absorbed into the pressure term. μ_t is the turbulent viscosity:

$$\mu_t = \rho C_\mu \frac{k^2}{\varepsilon} \tag{6}$$

The turbulent kinetic energy k and its dissipation rate ε are solved by the following transport equations, respectively.

$$\frac{\partial \rho k}{\partial t} + \frac{\partial \rho \overline{u}_j k}{\partial x_j} = \frac{\partial}{\partial x_j}\left[\left(\frac{\mu_t}{\sigma_k}\right)\frac{\partial k}{\partial x_j}\right] + P_k - \rho\varepsilon + f_k \tag{7}$$

$$\frac{\partial \rho\varepsilon}{\partial t} + \frac{\partial \rho \overline{u}_j \varepsilon}{\partial x_j} = \frac{\partial}{\partial x_j}\left[\left(\frac{\mu_t}{\sigma_\varepsilon}\right)\frac{\partial \varepsilon}{\partial x_j}\right] + C_{1\varepsilon}^* \frac{\varepsilon}{k}P_k - C_{2\varepsilon}\frac{\rho\varepsilon^2}{k} + f_\varepsilon \tag{8}$$

$$P_k = -\rho\left(\frac{\partial \overline{u}_i}{\partial x_j} + \frac{\partial \overline{u}_j}{\partial x_i}\right)\left(\frac{\partial \overline{u}_i}{\partial x_j}\right) \tag{9}$$

$$C_{1\varepsilon}^* = C_{1\varepsilon} + (C_{2\varepsilon} - C_{1\varepsilon})\frac{l_m}{l_{max}} \tag{10}$$

where P_k is the production of turbulent kinetic energy; f_k and f_ε are the user-defined source terms; $C_{1\varepsilon}, C_{2\varepsilon}, C_\mu, \sigma_k$ and σ_ε are the model constants ($C_{1\varepsilon} = 1.44, C_{2\varepsilon} = 1.92, C_\mu = 0.09, \sigma_k = 1.0, \sigma_\varepsilon = 1.11$ (Richards and Hoxey, 1993; Apsley and Castro, 1997; Castorrini et al., 2021); l_m denotes the turbulence length scale ($l_m = C_\mu^{3/4} k^{3/2}/\varepsilon$); and l_{max} represents the maximum turbulence length scale. When $l_m \ll l_{max}$ (i.e., near the ground surface), the value of the modified parameter $C_{1\varepsilon}^*$ is almost identical to $C_{1\varepsilon}$, and hence the equations are in accordance with the standard k-ε model. On the contrary, if l_m approaches l_{max}, the difference between source and sink terms in the ε equation becomes negligible based on the local equilibrium assumption (i.e., $P_k = \rho\varepsilon$).

2.3. LES model

In the LES model, the SGS Reynolds stress τ_{ij} is represented as follows:

$$\tau_{ij} = -\rho \overline{u_i'' u_j''} = 2\mu_{SGS}\overline{S}_{ij} - \frac{2}{3}\rho k_{SGS}\delta_{ij} \tag{11}$$

where μ_{SGS} is the SGS eddy viscosity and is determined from the SGS kinetic energy k_{SGS} by the following equation:

$$\mu_{SGS} = \rho C_k \overline{\Delta}\sqrt{k_{SGS}} \tag{12}$$

$$k_{SGS} = \frac{1}{2}\tau_{kk} = \frac{1}{2}\left(\overline{u_k u_k} - \overline{u}_k \overline{u}_k\right) \tag{13}$$

where $\overline{\Delta}$ is the grid-filter width based on the cell volume ($\overline{\Delta} = V^{1/3}$), and k_{SGS} is solved by the following transport equation (Yoshizawa and Horiuti, 1985):

$$\frac{\partial \rho k_{SGS}}{\partial t} + \frac{\partial \rho \overline{u}_j k_{SGS}}{\partial x_j} = -\tau_{ij}\frac{\partial \overline{u}_i}{\partial x_j} - C_\varepsilon \frac{\rho k_{SGS}^{3/2}}{\overline{\Delta}} + \frac{\partial}{\partial x_j}\left[(\mu + \mu_{SGS})\frac{\partial k_{SGS}}{\partial x_j}\right] \tag{14}$$

It should be noted that the one-equation eddy viscosity SGS model (Deardorff, 1973; Moeng, 1984; Wyngaard, 2004) can overcome the inadequacies of algebraic eddy viscosity SGS models caused by the local balance assumption, which may occur in cases of high Reynolds number flows and/or coarse grid resolution. The model constants are set as $C_k = 0.0472$ and $C_\varepsilon = 1.048$.

3. Model validation

In Section 3.1, the reliability of the LLS k-ε model in reproducing the neutral engineering ABL flow over flat terrain is first validated through a comparison with field observation data. The accuracy of the LLS k-ε
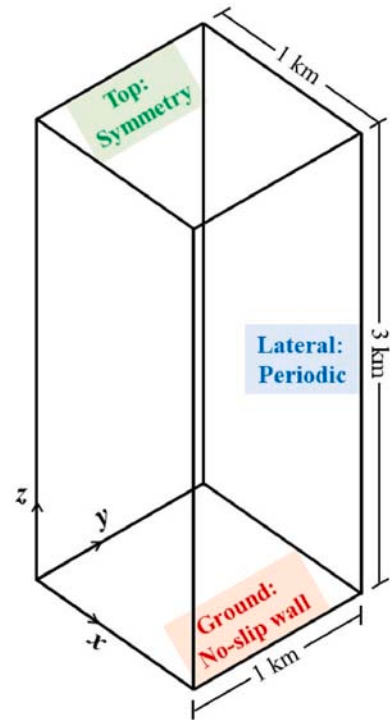

Fig. 1. Computational domain for the neutral engineering ABL flow over flat terrain by RANS simulations.

Table 1
Grid arrangements for RANS simulations of the neutral engineering ABL flow over flat terrain.

Case	$\Delta x, \Delta y$ (m)	Δz_{min} (m)	Vertical growth ratio	Grid number ($N_x \times N_y \times N_z$)
Grid-1	100	10	1.05	$10 \times 10 \times 50$
Grid-2	100	20	1.05	$10 \times 10 \times 50$
Grid-3	100	40	1.05	$10 \times 10 \times 50$

model for predicting the turbulent flow over a three-dimensional rough hill is subsequently validated by experimental results in Section 3.2.

3.1. Modeling neutral engineering ABL flow over flat terrain

The computational domain covers 1 km × 1 km × 3 km in the longitudinal (x), lateral (y) and vertical (z) directions, respectively. Ten grid cells are uniformly distributed in the longitudinal and lateral directions ($\Delta x = \Delta y = 100\,m$). To examine the sensitivity of grid discretization, the height of the cells nearest to the ground (Δz_{min}) changes from 10 m to 40 m. The details of the grid independence test are given in Table 1. As shown in Fig. 1, the periodic condition is employed for all lateral boundaries to consider wind veer effects caused by the Coriolis force. The no-slip condition is applied at the bottom surface, in which the k_s-type wall function is adopted to consider the ground roughness. The symmetry condition is utilized at the top of the domain.

In regard to the space discretization, the second-order linear-upwind scheme and the second-order limited linear scheme are adopted for the convection terms in the momentum equations and turbulence transport equations, respectively And the linear scheme is applied for the diffusion terms with the explicit-orthogonal correction. The SIMPLE algorithm is employed for the pressure-velocity coupling. The under-relaxation factors are specified as the value of 0.3 for pressure and 0.7 for other prognostic variables. To ensure the statistical convergence of the RANS simulations, the scaled residuals of all variables are reduced to the order of 10^{-6}. The specific RANS simulation parameters used for the Leipzig test case are provided in Table 2. It should be mentioned that the roughness length z_0 employed for the present RANS simulation is in accordance with many previous studies (Detering and Etling, 1985; Apsley and Castro, 1997; Koblitz et al., 2015; Feng and Gu, 2020), however, it is different from the other authors' (Hess and Garratt, 2002a) correction of this to a more physical value (0.14m) based on the Leipzig tower surroundings.

The vertical profiles of mean wind speed and wind veering angle predicted by the LLS k-ε model with different grid resolutions are shown in Fig. 2. It is demonstrated that the influence of grid resolution on the

vertical wind profiles reproduced by the LLS k-ε model is almost negligible. In general, the simulation results are in favorable agreement with field observation data. As illustrated in Fig. 2(a), both the ABL depth and the wind speed maxima in the upper ABL associated with its capping inversion are accurately captured by the LLS k-ε model with an appropriate *priori* value of l_{max}. Moreover, the mean wind veering angle is reasonably estimated by the LLS k-ε model after the Coriolis term is incorporated into the momentum equations, as depicted in Fig. 2(b).

Although the numerical results using an appropriate *priori* value of l_{max} or the formula proposed by Blackadar (1962) show good agreement with the Leipzig data (Lettau, 1950), it cannot reflect the impact of different terrain roughness on the vertical distributions of mean wind speed and direction in neutral atmospheric conditions. Therefore, a new formula for l_{max} will be proposed in Section 4.2.

3.2. Modeling turbulent flow over a three-dimensional rough hill in wind tunnel scale

The geometrical function of a three-dimensional hill with a rough surface of $z_0 = 0.3$ mm is expressed as: $z(x,y) = h\,cos^2\pi(x^2 + y^2)\,/2L$ with $h = 40$ mm and $L = 100$ mm in wind tunnel scale. Accordingly, the mean hill slope θ_s ($= tan^{-1}(h/2L)$) equals 21.8°. The dimension of the computational domain is set as $(L_x, L_y, L_z) = (60h, 20h, 22.5h)$. The non-uniform grid arrangement with 100 and 33 nodes is adopted in x and z directions, respectively. Additionally, the uniform grid arrangement with 29 nodes is applied in the y direction. With regards to the boundary conditions, the profiles of mean wind speed, turbulent kinetic energy and turbulence dissipation rate derived from the wind tunnel test for undistributed flow (Ishihara et al., 2001) are imposed as the inflow boundary, while the outflow condition is applied at the outlet boundary and the symmetry condition is employed at the upper and lateral boundaries. Both the numerical schemes and the convergence criteria utilized in Section 3.2 are kept the same as those in Section 3.1.

Profiles of mean velocity components and turbulent kinetic energy around the hill are presented in Fig. 3. The mean velocity components are normalized by the freestream velocity U_{ref} ($= 5.9$ m/s), while the turbulent kinetic energy is normalized by the square of the freestream velocity U_{ref}^2. Overall, the turbulent statistics predicted by the LLS k-ε model show acceptable agreement with those from the experiment. As illustrated in Fig. 3(a), both the speed-up features at the hillcrest and the flow separation and reattachment behind the hill are reasonably reproduced by this model. In contrast to the mean streamwise velocity, Fig. 3(b) shows that the mean vertical velocity is not strongly disturbed
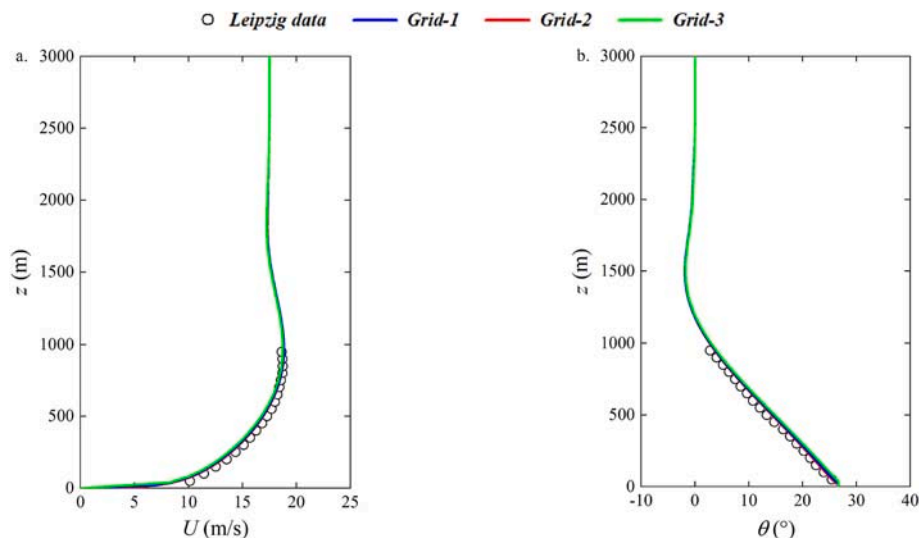
Table 2
RANS simulation parameters for the Leipzig test case.

Test case	Geostrophic wind speed U_g (ms^{-1})	Coriolis parameter f_c (s^{-1})	Roughness length z_0 (m)	Maximum length scale l_{max} (m)
Leipzig	17.5	1.13×10^{-4}	0.3	36

Fig. 2. Comparison of profiles of (a) mean wind speed and (b) mean wind veering angle predicted by the LLS k-ε model using different grid arrangements.
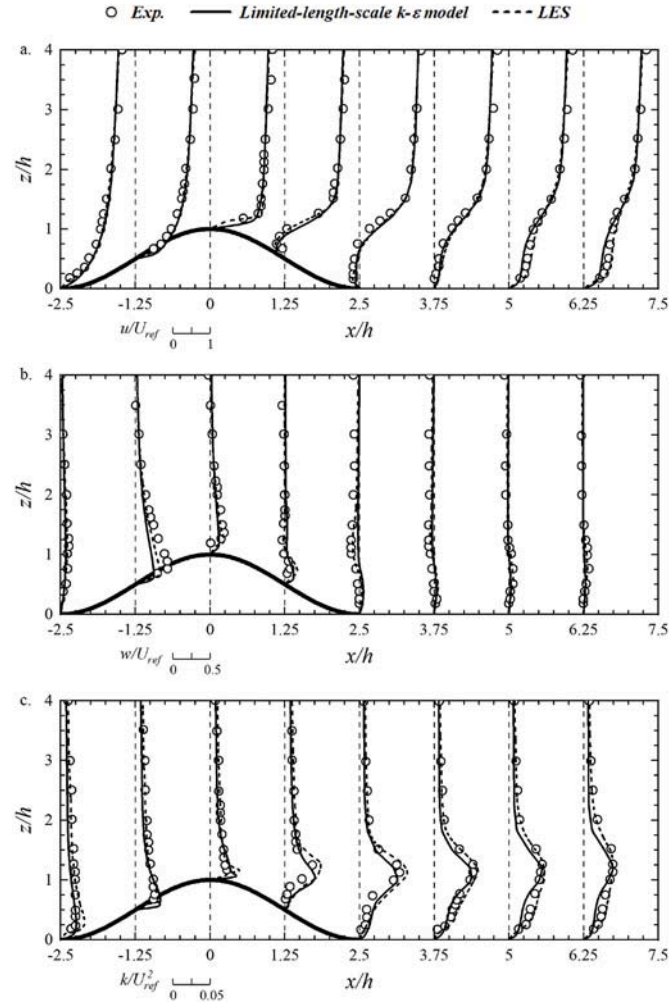
Fig. 3. Comparison of predicted and measured turbulent statistics: (a) mean streamwise velocity, (b) mean vertical velocity and (c) turbulent kinetic energy in the central plane of the hill.

by the hill. As depicted in Fig. 3(c), the magnitude of turbulent fluctuations is significantly enhanced on the lee slope, and the location of the maximum turbulence energy is marginally elevated as the wind flows downstream. Moreover, it should be noted that the vertical profiles of mean velocities and turbulence kinetic energy predicted by LES also show good agreements with experimental data, as illustrated in Fig. 3.

4. A new formula for maximum turbulence length scale

To reproduce neutral ABL flows over flat terrain with different surface roughness considering the Coriolis effects, a new formula to determine l_{max} is proposed for the LLS k-ε model in this section. Section 4.1 introduces the basic settings of numerical simulations, and a novel formulation for l_{max} is put forth based on LES simulations in Section 4.2.

4.1. Numerical settings

The full-scale LES simulations with a one-equation model for SGS kinetic energy are performed in this study. A source term $\rho f_c \varepsilon_{ij3}(G_j - \overline{u}_j)$ for the representation of Coriolis effects is incorporated into the momentum equations. The size of the computational domain is defined as length $(L_x) \times$ width $(L_y) \times$ height $(L_z) = 1$ km $\times$ 1 km $\times$ 3 km to avoid inertial oscillation effects and reduce computational costs. Additionally, it should be noted that the turbulence statistics within the neutral engineering ABLs (lacking any temperature inversion) are negligibly affected by the domain size after the wind field reaches a statistically steady state (Jiang et al., 2018; Lu and Li, 2022). To ensure a resolution-independent solution for each type of terrain roughness, a grid refinement study is carried out for three different horizontal and vertical grid resolutions, respectively. The details of the grid arrangements for the LES simulations are given in Table 3. As shown in Fig. 4, similar consistency among the Grid-2, Grid-3 and Grid-5 is found for the mean wind profiles, thus Grid-3 is adopted in the following calculations to reduce computational cost without compromising accuracy.

The boundary conditions for LES simulations are identical to those for RANS simulations in Section 3.1. The implicit backward scheme is employed for the unsteady term, and the central difference scheme is applied to the convection and viscous terms. The PISO coupling algorithm is chosen for the present simulations. To balance the numerical accuracy and stability of the unsteady simulations, a time-step size of $\Delta t = 0.25$ s is specified to limit the maximum Courant-Friedrichs-Lewy number to less than 1 in each LES calculation. Moreover, boundary layer depth (H) and friction velocity (u_*) are computed based on data extracted from the vertical centerline of the domain, as the variation of boundary layer depth and friction velocity reach approximate plateau, indicating a fully developed boundary layer and a stable near-wall flow field. In this study, the boundary layer depth is defined as the height at which the total momentum flux drops less than 5% of the ground value (Coleman, 1999; Berthaut-Gerentes and Delaunay, 2015; Lu and Li, 2022). All LES simulations in the present study are calculated for 2×10^5 s (8×10^5 time steps in total) and the data in the last 1×10^5 s are extracted for the following analysis. A statistically stationary condition for the sampling period is examined by calculating relative errors in mean wind speed, mean wind veering angle and turbulence intensity at the vertical centerline of the domain. The time sampling error is evaluated by the discrepancies of the mean wind and turbulent quantities from 1×10^5 s to 1×10^5 s $+ T/2$ and that from 1×10^5 s $+ T/2$ to 1×10^5 s $+ T$, where T is the sampling period ($T = 1 \times 10^5$ s). It is found that the relative errors of mean wind and turbulence quantities for each case are less than 2%, as shown in Fig. 5. Moreover, it should be noted that all simulation cases were run for a sufficiently long large-eddy turnover time ($t^* = L_z/u_*$) of approximately at least 20 to ensure statistical convergence. Specific LES simulation parameters used for the neutral ABL flows over different terrain exposures are summarized in Table 4.

Regarding the RANS simulations, a slender computational domain which is the same as the LES simulations is adopted. In addition, the boundary conditions and the discretization schemes of all spatial gradients used for all RANS cases in this section are identical to those in Section 3.1. The numerical convergence is typically achieved after 10^4 iterations, and the scaled residuals of all physical variables are less than 10^{-5}.

Table 3
Grid arrangements for LES simulations of neutral ABL flows over different terrain exposures.

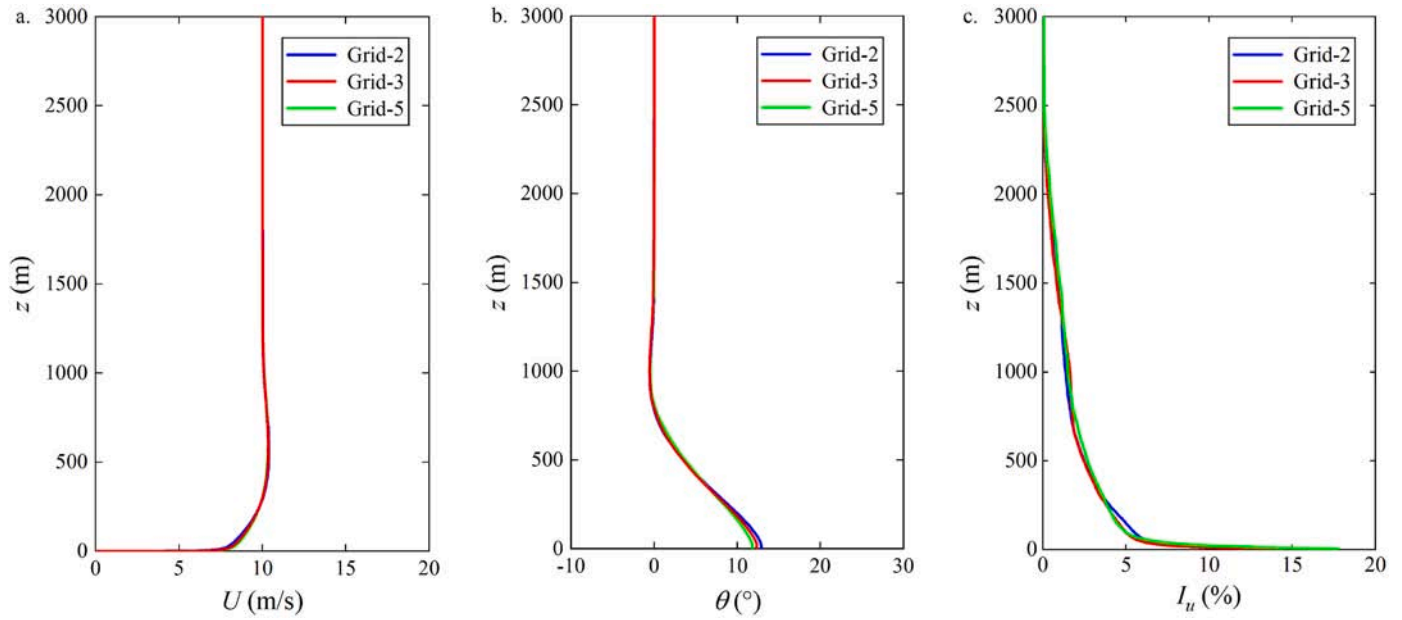| Case	$\Delta x, \Delta y$ (m)	Δz_{min} (m)	Vertical growth ratio	Grid number ($N_x \times N_y \times N_z$)
Grid-1	10	2	1.03	$100 \times 100 \times 120$
Grid-2	10	0.5	1.03	$100 \times 100 \times 180$
Grid-3	10	1	1.03	$100 \times 100 \times 150$
Grid-4	20	1	1.03	$50 \times 50 \times 150$
Grid-5	5	1	1.03	$200 \times 200 \times 150$

Fig. 4. Comparison of profiles of (a) mean wind speed, (b) mean wind veering angle and (c) turbulence intensity for the neutral ABL flow over a flat surface ($z_0 = 0.0001$ m) by LES using different grid arrangements.
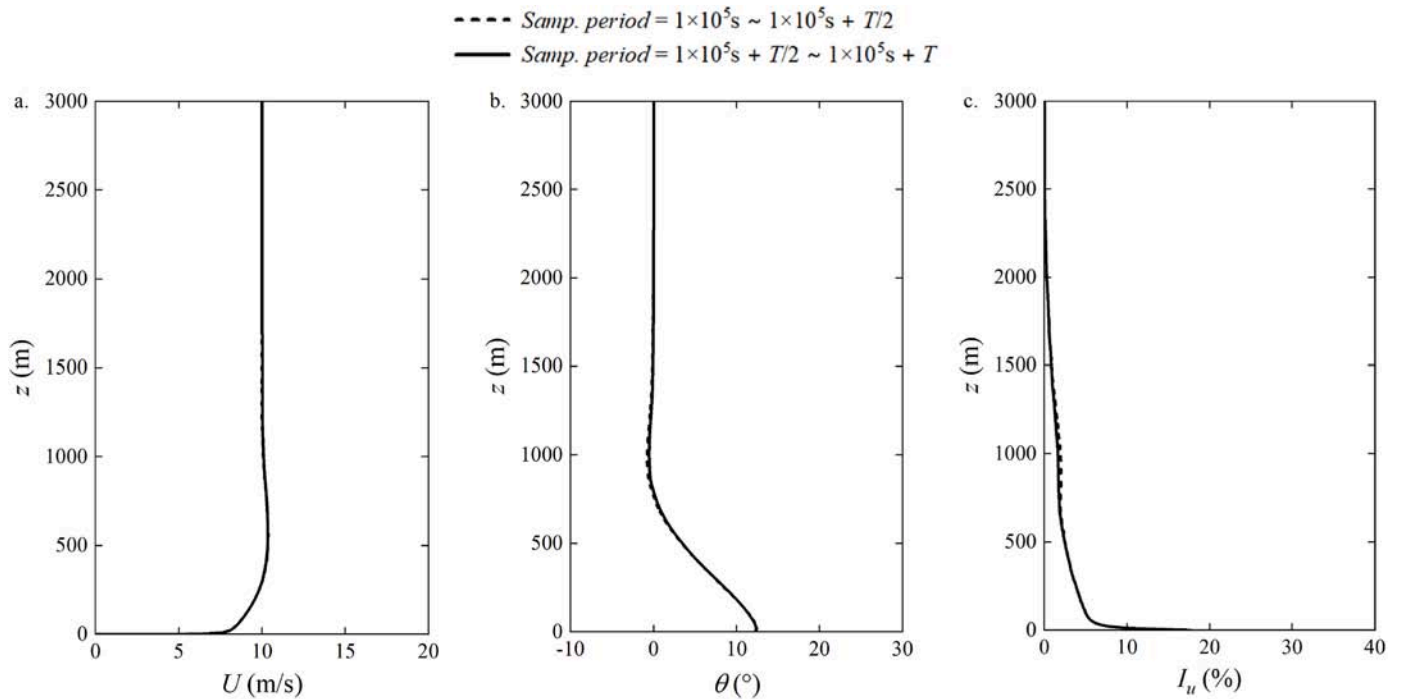

Fig. 5. Comparison of profiles of (a) mean wind speed, (b) mean wind veering angle and (c) turbulence intensity for the neutral ABL flow over a flat surface ($z_0 = 0.0001$ m) by LES under different sampling periods.

4.2. Proposal of formula for maximum turbulence length scale

Profiles of mean wind speed, mean wind veering angle and turbulence intensity for neutral ABL flows under different terrain exposure conditions are depicted in Fig. 6. As shown in Fig. 6(a), the increase in the gradient height of neutral ABL flows is attributed to the increasing surface roughness. In addition, in the case of rough terrain, lower wind speed near the ground is exhibited. Furthermore, the influence of exposure roughness was shown to decrease with increasing height From Fig. 6(b), it can be seen that the variation of mean wind direction

throughout the neutral ABL is strongly dependent on the upstream roughness, which is in good accordance with previous studies (Hess and Garratt, 2002b; Lindvall and Svensson, 2019). The maximum value of wind veering angle is observed to be in the proximity of the ground surface, which varies from $10°$ to $20°$ for different terrain roughness. It is found that the wind veer effects induced by the Coriolis force are stronger in the case of rougher terrain, implying that wind veering phenomena should be paid much more attention to as the surface roughness increases. Furthermore, the turbulence fluctuations above the terrain become more significant in the cases with larger surface

Table 4

Simulation parameters for LES simulations of neutral ABL flows over different terrain exposures.

Case	U_g (m s^{-1})	f_c (s^{-1})	z_0 (m)	Terrain exposures
1	10	10^{-4}	0.0001	Open sea
2	10	10^{-4}	0.001	Very flat terrain (no vegetation & obstacles)
3	10	10^{-4}	0.01	Open terrain (grassland, few obstacles)
4	10	10^{-4}	0.1	Suburban terrain (low crops, occasional large obstacles)
5	10	10^{-4}	0.3	Suburban terrain (high crops, scattered obstacles)

roughness, which can be seen in Fig. 6(c).

Fig. 7 illustrates the relationship between the normalized gradient height ($z_g^* = z_g/(U_g/f_c)$) and the surface Rossby number ($Ro_s = U_g/f_c z_0$), in which the double-logarithmic coordinate system is adopted. This study defines the gradient height as the height where wind speed attains the gradient value, which is a commonly accepted definition used in many wind load codes and standards (AIJ-RLB-2015, ASCE 7–16, GB50009-2012). As the surface Rossby number Ro_s increases, the normalized gradient height z_g^* is seen to be decrease. Additionally, it should be noted that the rate of decrease of z_g^* tends to slow down with increasing Ro_s. For quantitative evaluation, a power-law formula is proposed to describe this non-linear dependency between Ro_s and z_g^* by fitting the numerical results obtained from LES simulations:

$$z_g^* = 0.014 log(Ro_s)^{-0.7} \tag{15}$$

For a given set of U_g, f_c and z_0, the mean wind speed profiles of neutral ABL flows are primarily determined by l_{max}. Specifically, the nominal ABL depth (gradient height) predicted by the LLS k-ε model is effectively controlled by l_{max} (van der Laan et al., 2020). Hence, it is of great necessity to further elucidate the correlation between z_g and l_{max} for a fixed value of U_g, f_c and z_0.

Based on the above analysis, the basic parameters (U_g, f_c and z_0) for reproducing the neutral ABL flows over different terrain exposures by the LLS k-ε model remain consistent with the corresponding LES simulations. Consequently, only l_{max} is a variable that needs to be determined
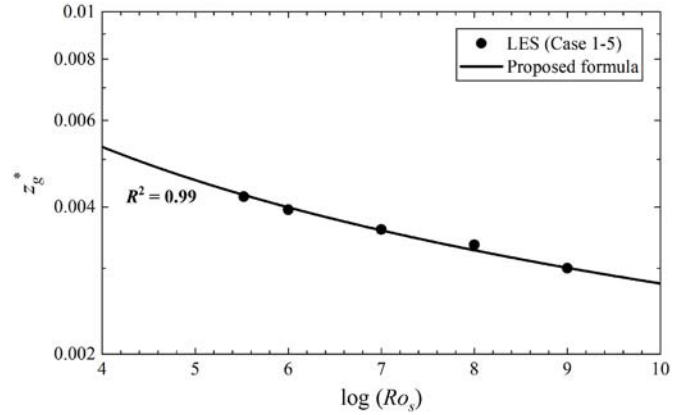

Fig. 7. Variation of the normalized gradient height z_g^* with surface Rossby number Ro_s.
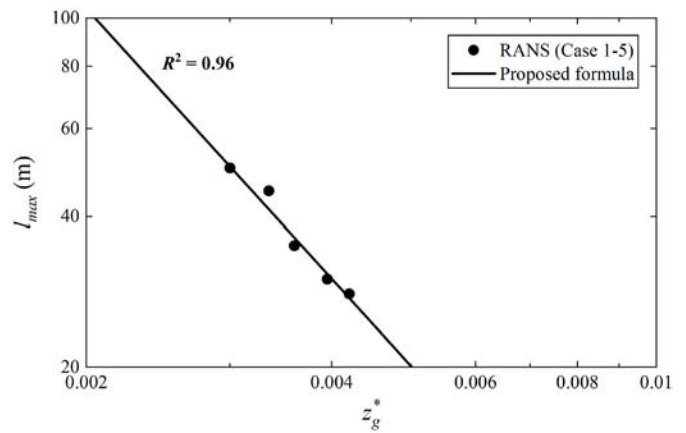

Fig. 8. Variation of the normalized gradient height z_g^* with maximum turbulence length scale l_{max}.
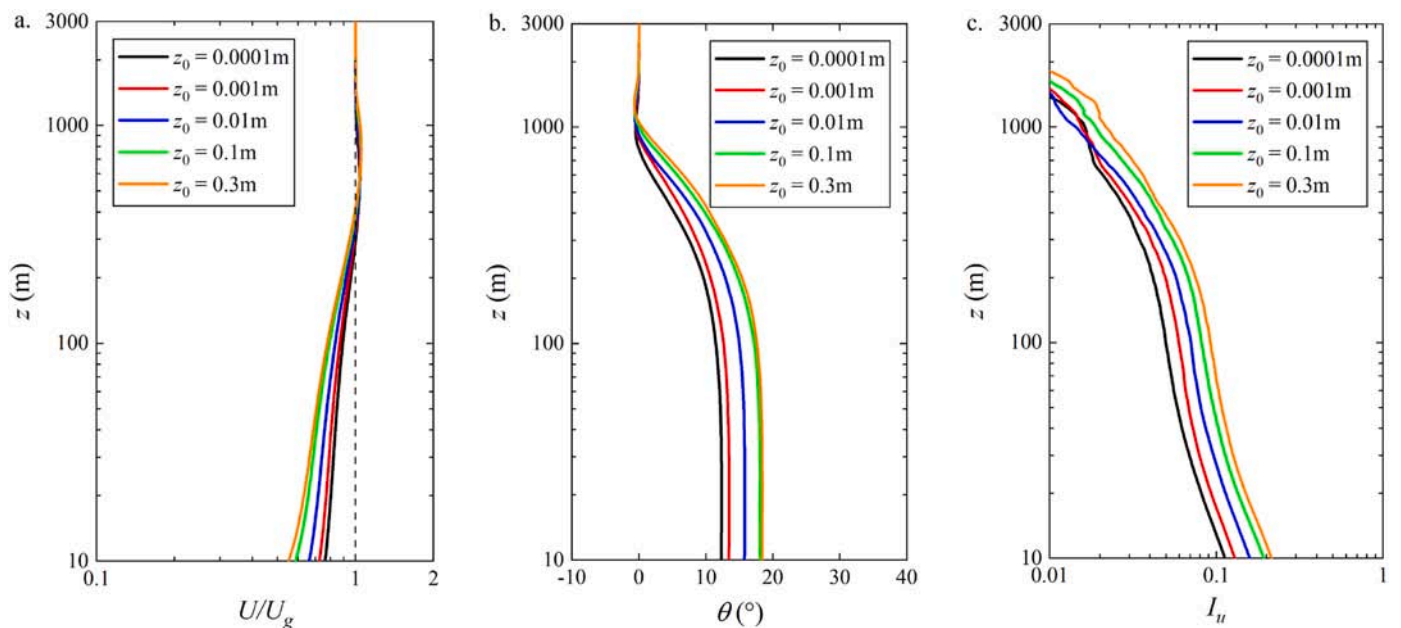

Fig. 6. Profiles of (a) mean wind speed, (b) mean wind veering angle and (c) turbulence intensity for neutral ABL flows over different terrain exposures predicted by LES.
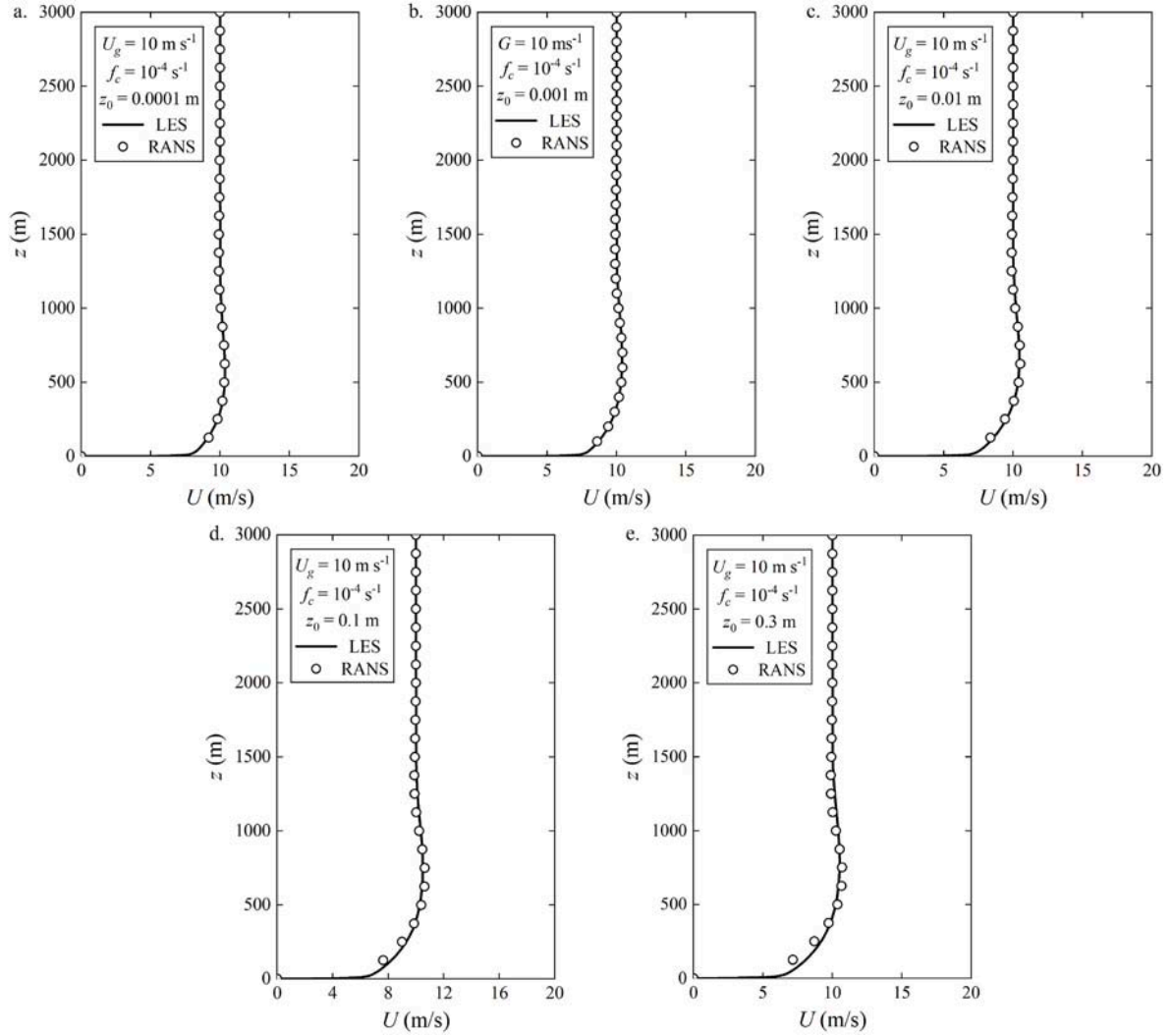
Fig. 9. Profiles of mean wind speed for neutral ABL flows over different terrain exposures predicted by RANS and LES: (a) $z_0 = 0.0001m$, (b) $z_0 = 0.001m$, (c) $z_0 = 0.01m$, (d) $z_0 = 0.1m$ and (e) $z_0 = 0.3m$.

for the RANS simulation of atmospheric flow over each specific exposure condition. The gradient height z_g of neutral ABL flows over different terrain exposures predicted by the above LES simulations is prescribed as the target value for the RANS simulations. To find out the optimal value of l_{max} for simulating atmospheric flows over flat terrain with different surface roughness, the trial-and-error approach is further adopted in the following RANS simulations. The most favorable l_{max} value for neutral ABL flows over different terrain exposures (from $z_0 = 0.0001$ m to $z_0 = 0.3$ m) are 50 m, 45 m, 35 m, 30 m, 28 m.

Accordingly, the relationship between z_g^* and l_{max} are plotted in the double-logarithmic coordinate system as depicted in Fig. 8, which can be reasonably described by the following formula:

$$l_{max} = 0.00145 \, [m] \times \left(z_g^*\right)^{-1.8} \tag{16}$$

It should be noted that the proposed formula (Eq. (14) and Eq. (15)). qualitatively resemble the expressions derived by van der Laan et al. (2020) based on the Rossby number similarity, in which l_{max} is inverse proportional to the ABL depth.

Combing Eq. (14) and Eq. (15), l_{max} can be rearranged into a new expression Eq. (16), which is a function of surface Rossby number ($Ro_s = U_g/f_c z_0$). Since z_0 is introduced into the novel formula for l_{max}, it is reasonable to conceive that the proposed formula can quantify the

impacts of different terrain roughness on the vertical mean wind profiles of neutral ABL flows.

$$l_{max} = 3.15 \, [m] \times log \, (Ro_s)^{1.26} \tag{17}$$

To validate the feasibility of the above proposed formula, the RANS simulations of neutral ABL flows over different terrain exposures are performed using the proposed formula for l_{max}. The gradient heights of neutral ABL flows over different terrain exposures predicted by the LLS k-ε model show good agreements with those obtained from the LES, in which the relative errors are less than 2%. Moreover, the mean wind speed profiles for the neutral ABL flows over different terrain exposures reproduced by the LLS k-ε model are very close to those predicted by LES simulations, as shown in Fig. 9.

5. Effects of Coriolis force on atmospheric flows over three-dimensional hills

In this section, the LLS k-ε model is adopted to investigate the effects of Coriolis force on atmospheric flows over three-dimensional hills with different hill slopes and height ratios. Section 5.1 outlines the major settings of the numerical simulations. The flow patterns and turbulent statistics are discussed in Section 5.2 and Section 5.3, respectively.
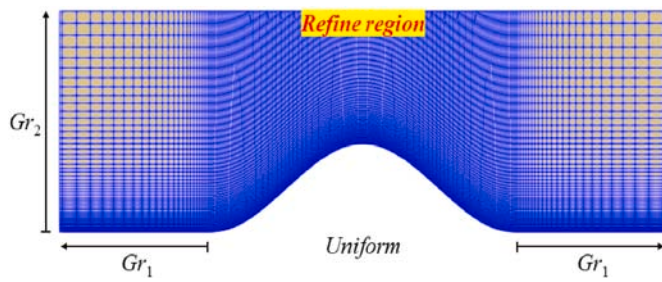
Fig. 10. Grid distributions around the three-dimensional hill.

5.1. Numerical settings

The computational domain has dimensions of $L_x \times L_y \times L_z = 16\,\text{km} \times 8\,\text{km} \times 9\,\text{km}$. The shape function of three-dimensional hills is defined as follows: $z_s(x, y) = h\,cos^2\pi(x^2 + y^2)/2L$. It should be noted that the domain width is large enough to alleviate the disturbance of periodic boundary conditions on flow fields over hills. Additionally, the blockage ratio is lower than 5% for each simulation case to avoid artificial flow acceleration. To accurately capture the turbulence characteristics around the hilly region, the local terrain-following grid refinement is adopted in this study, as shown in Fig. 10. The growth ratio Gr_1 and Gr_2 is chosen as 1.1 and 1.05, respectively. Regarding the grid sensitivity analysis of the numerical model, three types of grid systems with different resolutions in the longitudinal direction are examined for the cases considering the Coriolis force. The details of the grid arrangements are presented in Table 5. Comparisons of the profiles of mean wind speed and turbulent kinetic energy predicted by RANS simulations with these three grid systems are demonstrated in Fig. 11. It is observed that the differences in mean wind and turbulence statistics among these three grid systems are almost negligible. Therefore, based on the grid sensitivity analysis, the grid system with intermediate resolution is employed for subsequent simulations.

The profiles of mean wind speed and turbulence properties derived from the precursor RANS simulation considering the Coriolis force are imposed as the inflow boundary for the cases with Coriolis effects, as shown in Fig. 12. To account for the effects of Coriolis force, the l_{max} is determined by the proposed formula (Eq. (16)), in which l_{max} is a function of U_g, f_c and z_0. Both the gradient wind speed and the gradient height in the cases with the Coriolis force are identical to those in the cases without the Coriolis force. In addition, the surface wind vector is perpendicular to the inlet plane for the cases considering the effects of Coriolis force. The outflow condition of zero-gradient is employed for

Table 5
Grid arrangements for RANS simulations of turbulent flows over three-dimensional hills.

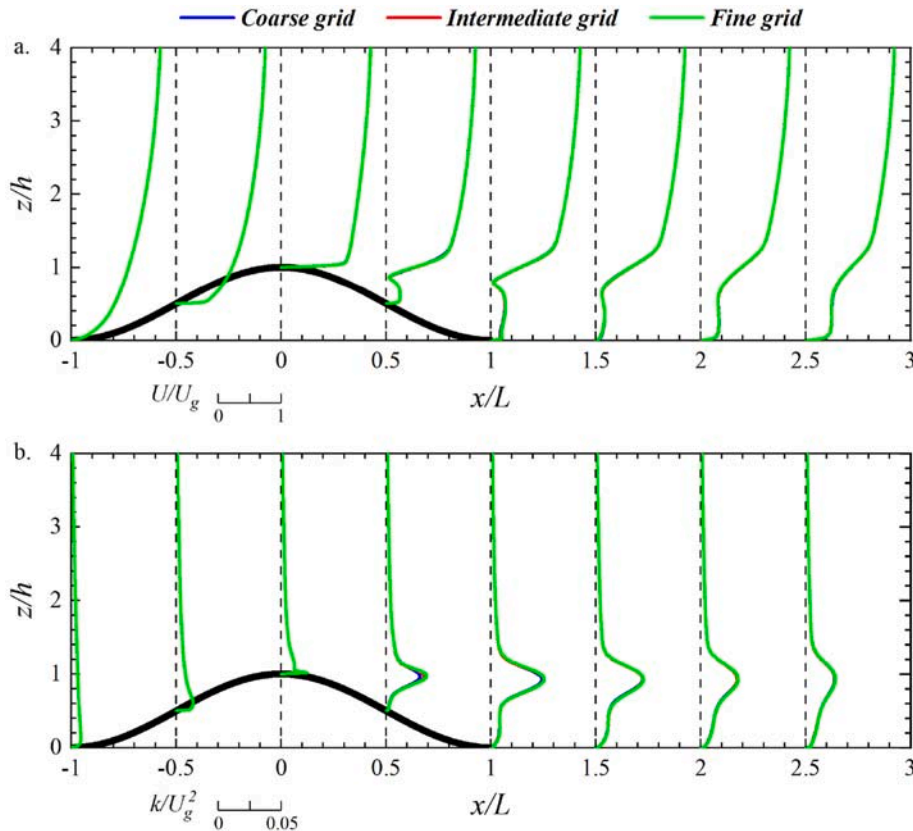| Grid	Horizontal resolution				Vertical resolution			Total number
	N_x	N_y	$\Delta x_{min}, \Delta y_{min}$ (m)	Gr_1	N_z	Δz_{min} (m)	Gr_2	
Coarse	180	160	20	1.1	100	2	1.05	2,880,000
Intermediate	225	205	15	1.1	100	2	1.05	4,612,500
Fine	300	280	10	1.1	100	2	1.05	8,400,000

Fig. 11. Comparison of normalized profiles of turbulent statistics for atmospheric flows over a three-dimensional hill ($\theta_s = 21.8°$, 200m high) by the LLS k-ε model using different grid arrangements: (a) mean wind speed and (b) turbulent kinetic energy in the central plane of the hill.
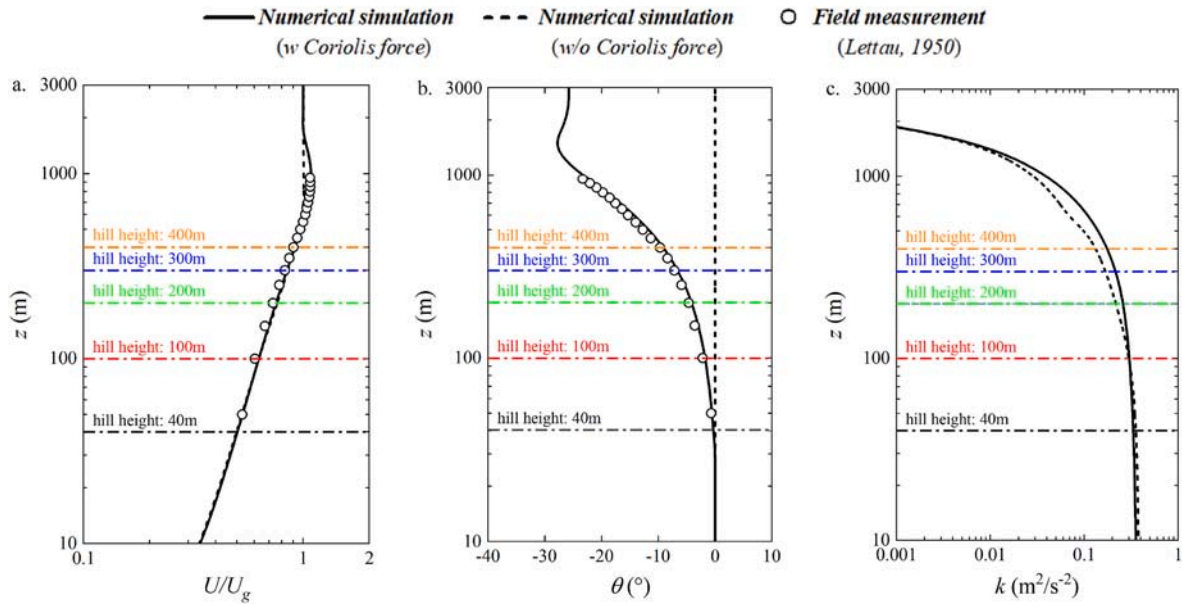
Fig. 12. Approaching flow conditions of turbulent flow modeling over three-dimensional hills with different hill slopes and height ratios: (a) mean wind speed, (b) mean wind veering angle and (c) turbulent kinetic energy.

Table 6
Numerical schemes for RANS simulations of atmospheric flows over three-dimensional hills.

Items	Numerical schemes
Convection term	u: Gauss linearUpwind
	k & ε: Gauss limitedLinear 1
Diffusion term	Gauss linear corrected
Gradient term	Gauss linear
Pressure-velocity coupling algorithm	SIMPLE

Table 7
Case settings for RANS simulations of atmospheric flows over three-dimensional hills.

Case	Three-dimensional hill				Whether the Coriolis force is considered
	L (m)	h (m)	Hill slope	Height ratio h/H	
1	100	40	21.8°	1/15	Yes
2	100	40	21.8°	1/15	No
3	250	100	21.8°	1/6	Yes
4	250	100	21.8°	1/6	No
5	500	200	21.8°	1/3	Yes
6	500	200	21.8°	1/3	No
7	750	300	21.8°	1/2	Yes
8	750	300	21.8°	1/2	No
9	1000	400	21.8°	2/3	Yes
10	1000	400	21.8°	2/3	No
11	2000	200	5.7°	1/3	Yes
12	2000	200	5.7°	1/3	No
13	1000	200	11.3°	1/3	Yes
14	1000	200	11.3°	1/3	No
15	250	200	38.7°	1/3	Yes
16	250	200	38.7°	1/3	No

the outlet and the symmetry condition is applied at the upper boundary and the periodic condition was adopted for the lateral boundaries to account for wind veer. For the lower boundary, the no-slip condition is employed and the surface roughness is modeled by a wall function.

To balance prediction accuracy and solution stability, the second-order linear-upwind scheme is adopted for the continuity and momentum equations. The second-order limited linear scheme is employed for the convective terms of the turbulence transport equations (Castorrini et al., 2021) and the second-order Gauss linear corrected scheme is applied for the discretization of diffusion term and the gradient term (Han and Stoellinger, 2020). Moreover, the SIMPLE algorithm is applied to deal with the pressure-velocity coupling in the following RANS simulations. Table 6 summarizes the numerical schemes utilized in this section. To comprehensively shed light on the coupling effects of Coriolis force, hill slopes and height ratios on atmospheric flows over three-dimensional hills, the main simulation settings for the following systematic study are outlined in Table 7, in which the ABL height is determined as its gradient value ($H = z_g \approx 600$ m).

5.2. Flow patterns

Fig. 13 presents the horizontal distributions of time-averaged velocity streamlines around 200 m high three-dimensional hills with gentle and steep slopes. When Coriolis effects are ignored, the mean flow streamlines are symmetrically distributed around hills with different slopes ($\theta_s = 11.3°, 21.8°$), as exhibited in Fig. 13(a) and (b). As the hill slope increases, a pair of secondary vortices with a three-way-encounter pattern is identified in the wake of the steep hill. However, in the cases that consider the Coriolis force, the wake centerline behind the gentle hill ($\theta_s = 11.3°$) and the steep hill ($\theta_s = 21.8°$) is deflected due to the existence of spanwise fluid motions. Additionally, as indicated in Fig. 13 (c) and (d), the wake deflection angle for the steep hill is greater than that of the gentle hill, implying a stronger wake veer effect in the steeper topography. Moreover, it is demonstrated that a pair of counter-rotating secondary vortices are developed on the lee slope of the steep hill.

Fig. 14 shows the vertical distribution of time-averaged velocity streamlines around 200 m high, three-dimensional hills with gentle and steep slopes. As demonstrated in Fig. 14(a) and (c), the Coriolis force does not exert a considerable influence on the fluid movement around a 200 m high three-dimensional gentle hill in the streamwise direction. Nevertheless, a significant reduction in the wake depth behind a 200 m high three-dimensional steep hill can be observed for the cases that consider Coriolis effects, which is displayed in Fig. 14(b) and (d). Furthermore, it is evident that the Coriolis force contributes to the recovery process of wake loss on the lee side of the three-dimensional steep hill.
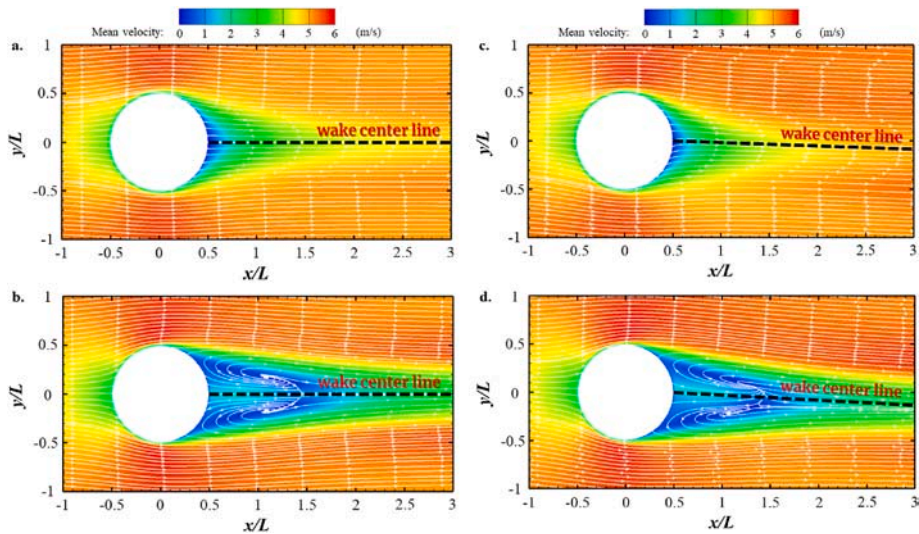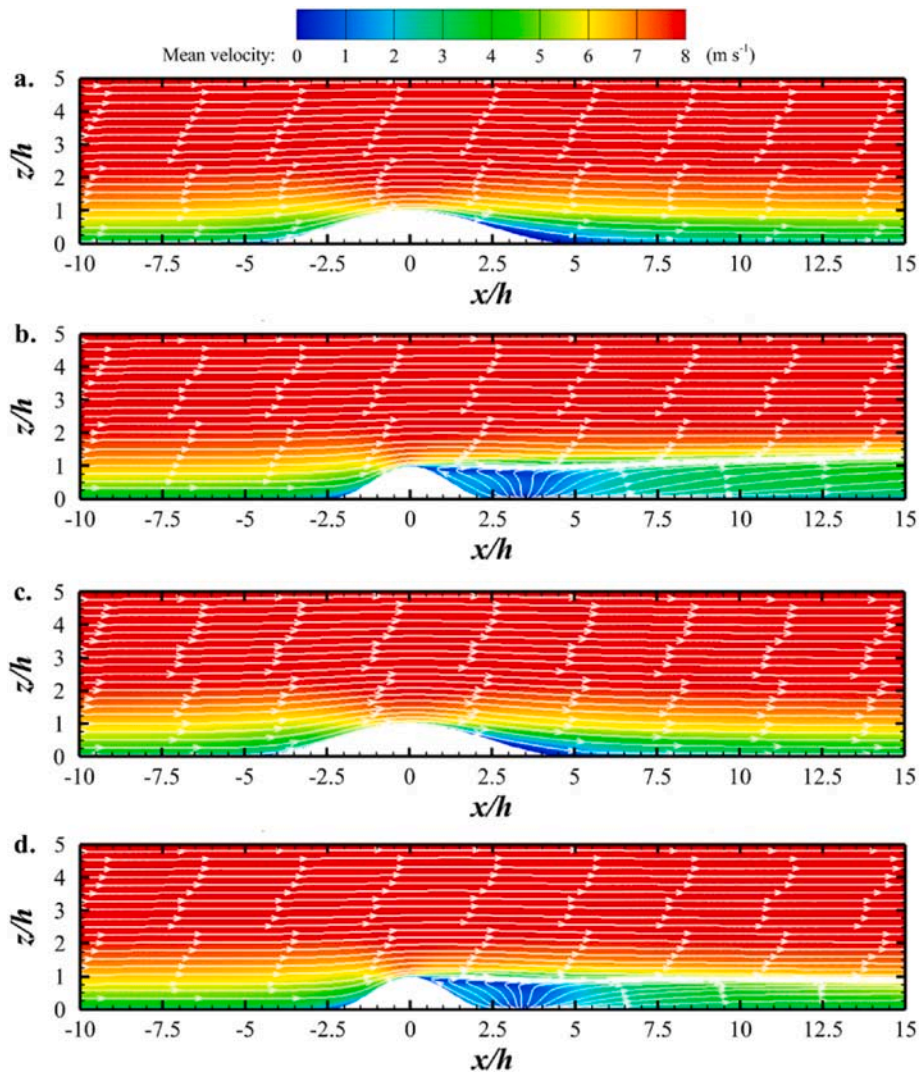
Fig. 13. Coupling effects of Coriolis force and hill slopes on the mean velocity streamlines over 200 m high three-dimensional hills at $z = 0.5h$ plane: (a) $\theta_s = 11.3°$, (b) $\theta_s = 21.8°$ (w/o Coriolis force), (c) $\theta_s = 11.3°$, (d) $\theta_s = 21.8°$ (with Coriolis force).
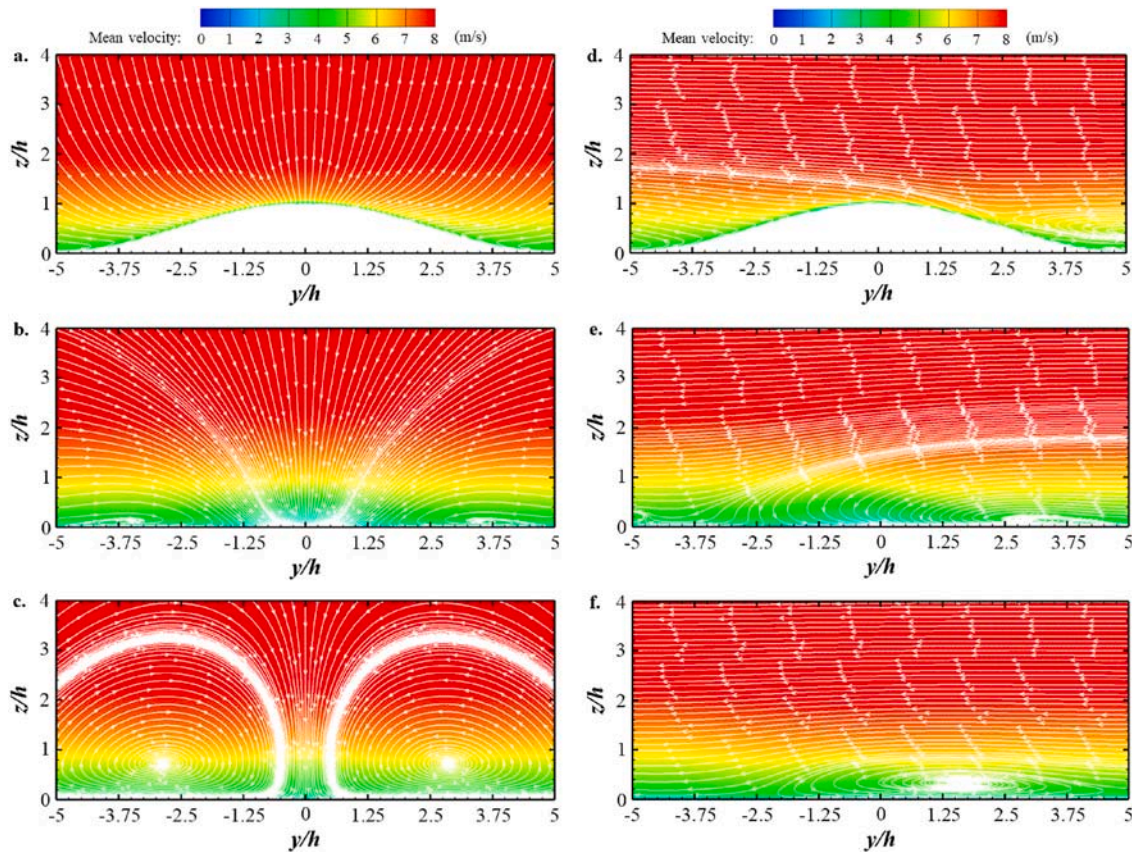

Fig. 14. Coupling effects of Coriolis force and hill slopes on the mean velocity streamlines over 200 m high three-dimensional hills at $y = 0$ plane: (a) $\theta_s = 11.3°$, (b) $\theta_s = 21.8°$ (w/o Coriolis force), (c) $\theta_s = 11.3°$, (d) $\theta_s = 21.8°$ (with Coriolis force).

Fig. 15. Effects of Coriolis force on the mean velocity streamlines over a 200 m high three-dimensional gentle hill ($\theta_s = 11.3°$) at several lateral planes: (a) $x = 0$, (b) $x = 1.5L$, (c) $x = 3L$ (w/o Coriolis force), (d) $x = 0$, (e) $x = 1.5L$, (f) $x = 3L$ (w Coriolis force).

Fig. 15 depicts mean velocity streamlines around a 200 m high three-dimensional gentle hill ($\theta_s = 11.3°$) at several representative lateral planes ($x/L = 0$, 1.5 and 3). When Coriolis effects are neglected, the streamlines at $x/L = 0$ plane are upward and outward, as illustrated in Fig. 15(a). Conversely, in the near-wake region ($x/L = 1.5$), the streamlines are mostly inward and downward. More interestingly, it is revealed from Fig. 15(b) that small-scale vortices are generated on both sides of the central plane in a symmetric manner. As the wind flow moves downstream ($x/L = 3$), the bilateral vortex pair is significantly enlarged as the uplifted vortex cores, as illustrated in Fig. 15(c). However, it is found that the mean flow patterns around the gentle hill are strongly affected by the Coriolis force. As revealed in Fig. 15(d), most streamlines are westward at the $x/L = 0$ plane owing to the presence of lateral wind shear. Additionally, large-scale vortices are formed on the windward side of the hill due to its blockage effects. Moreover, on the leeward side, a single near-wall vortex is formed on one side and its scale is gradually enlarged with downstream distance, which is shown in Fig. 15(e) and (f).

To gain better insights into Coriolis effects on mean flow patterns around hills with different slope features, the time-averaged velocity streamlines around a 200 m high three-dimensional steep hill ($\theta_s = 21.8°$) at the same lateral planes are shown in Fig. 16. At the plane of $x/L = 0$, the spatial distributions of streamlines over the steep hill are analogous to that of the gentle hill for both cases with and without Coriolis force, see Fig. 16(a) and (d). Nevertheless, the mean velocity streamlines show large differences in the wake of the steep hill since the flow separates on the lee slope of steep topography. As the flow moves downstream, despite a weak upwash in the center plane, the near-wake structures are predominantly characterized by the strong downwash motion, as observed in Fig. 16(b). Furthermore, it is revealed from Fig. 16(c) that the far-wake patterns are significantly changed from the

view of the increasing size of central trailing vortices and the gradual formation of near-ground vortices outside the central region. When the Coriolis force is considered, the wake flow patterns around the steep hill are significantly dissimilar to those of the gentle hill. It is illustrated in Fig. 16(e) that the trailing vortices are asymmetrically generated in the near-wake region. As the flow moves downstream, the large trailing vortices are driven by the spanwise flow and shifted to one side from the central region, while the small trailing vortices are formed in the near-wall region, which is demonstrated in Fig. 16(f).

5.3. Turbulent statistics

Profiles of mean velocity and turbulent kinetic energy around 200 m high hills ($h/H = 1/3$) with different hill slopes ($\theta_s = 5.7°$, 11.3°, 21.8°, 38.7°) are shown in Fig. 17(a) and (b). On the upstream side, the negligible influences of the Coriolis force on the vertical distributions of mean velocity over three-dimensional hills are demonstrated regardless of hill slopes. Additionally, the mean velocity distributions on the downstream side of gentle hills ($\theta_s = 5.7°$, 11.3°) are shown to be largely insensitive to the Coriolis force. However, the wake velocity deficit in the center plane of steep hills ($\theta_s = 21.8°$, 38.7°) recovers faster for the cases with the Coriolis force, as depicted in Fig. 17(a). To quantitively evaluate the wake deficit recovery, the normalized velocity deficit ($\Delta U/U_{inflow}$) in the streamwise direction downwind of the three-dimensional hills is used in the following analysis, where $\Delta U = U_{inflow} - U$ is the mean velocity deficit, and U_{inflow} is the mean inflow velocity. In the far-wake region ($x = 3.5L$) of the three-dimensional steep hill, it is found that the magnitude of the normalized velocity deficit is approximately 15% greater in the case where the Coriolis force was neglected. In contrast to gentle hills, more intense turbulence fluctuations are observed on the lee side of steep hills due to the presence of stronger
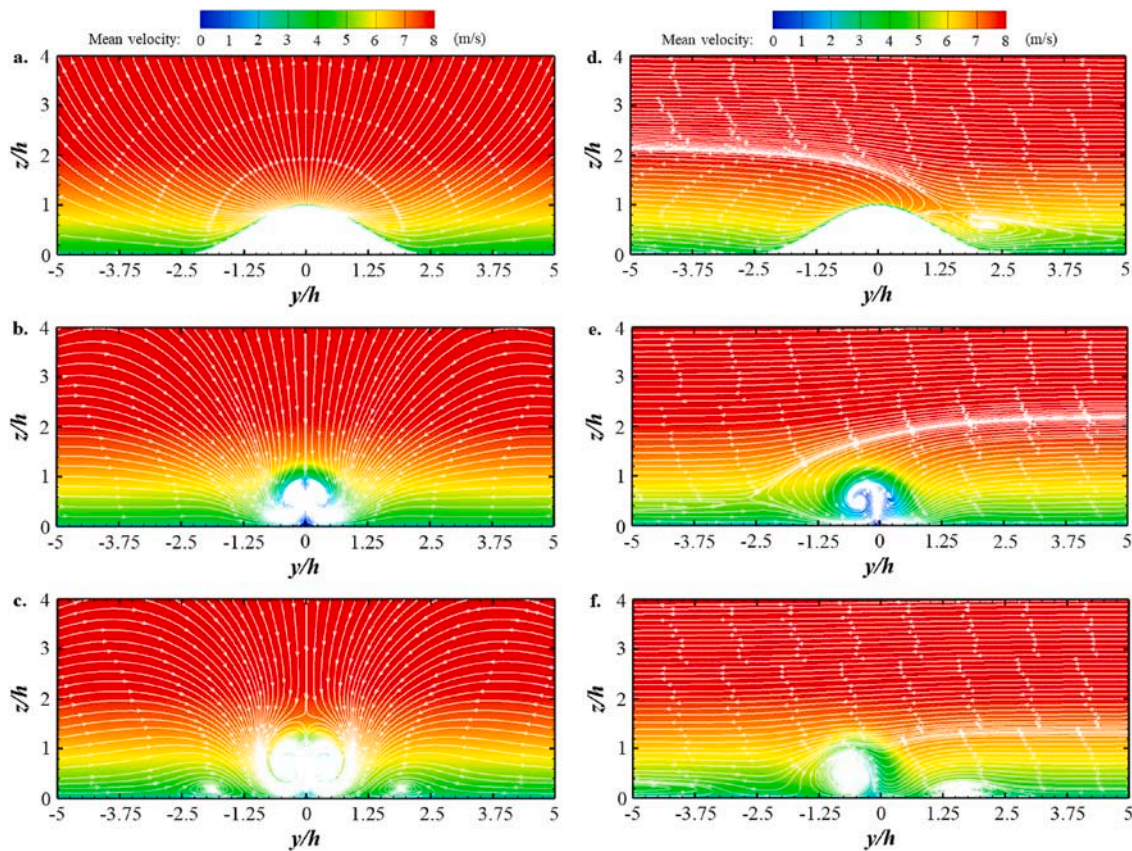
Fig. 16. Effects of Coriolis force on the mean velocity streamlines over a 200 m high three-dimensional steep hill ($\theta_s = 21.8°$) at several lateral planes: (a) $x = 0$, (b) $x = 1.5L$, (c) $x = 3L$ (w/o Coriolis force), (d) $x = 0$, (e) $x = 1.5L$, (f) $x = 3L$ (w Coriolis force).

separated flow. Moreover, it is found that the total kinetic energy of wake turbulence in the center plane of steep hills is about 5% higher for the cases with the Coriolis force, as illustrated in Fig. 17(b). As discussed by Qian and Ishihara (2022), the wake deflection induced by the Coriolis force is a combined action of wind veer in the ambient flow and added turbulence in the wake. The added turbulent eddy viscosity is generated from the shear of the hill-induced wake. In the wake of steep hills, the production of turbulent kinetic energy and the turbulence momentum flux are enhanced by the lateral wind shear associated with the Coriolis force. This further leads to a larger flow entrainment and a faster wake recovery compared to the cases that neglect Coriolis effects.

To deepen the understanding of Coriolis effects on the spatial distributions of turbulent statistics over gentle and steep hills, the vertical profiles of mean velocity and turbulent kinetic energy at several representative lateral planes are presented in Fig. 18. In the cases without the Coriolis force, it is found that the turbulent statistics in the wake of three-dimensional hills with different hill slopes are symmetrically distributed on the two sides of the central plane. However, an asymmetrical distribution of turbulent statistics is observed on the lee side of steep hills for the cases that consider the Coriolis force, implying the formation of skewed spatial structures of the hill wake. Furthermore, it is demonstrated that a portion of turbulent kinetic energy is transported away from the center region to the lateral side due to the wind veer effects caused by the Coriolis force.

Fig. 19(a) shows the vertical distributions of mean velocity for steep hills ($\theta_s = 21.8°$) with different height ratios ($h/H = 1/15, 1/6, 1/3, 2/3$). The effective Rossby number Ro_h ($= U_g/fh$) is introduced hereafter for the following discussion. For the small height ratios ($h/H = 1/6, 1/15$), the mean velocity and the turbulent kinetic energy around steep hills in the cases with Coriolis force are almost consistent with those without Coriolis force. However, it is demonstrated that the profiles of

turbulent statistics around steep hills with large height ratios ($h/H = 2/3, 1/3$) are significantly affected by the Coriolis force. As h/H increases, the corresponding Ro_h decreases, therefore it is reasonable to assume that the vertical wind veer effect associated with the Coriolis force becomes much more remarkable. This further leads to a substantial enhancement of flow entrainment and the rapid recovery of velocity deficit in the hill wake for the cases with small Ro_h. In the far-wake region of a 400 m high three-dimensional steep hill ($h/H = 2/3$), it is ascertained that the normalized velocity deficit exhibits an increase of roughly 35% when the Coriolis force is not taken into consideration. Moreover, as depicted in Fig. 19(b), the wake turbulence for the steep hills with large h/H are strongly affected by the Coriolis force, while it is not true for cases with small h/H.

Fig. 20 illustrates the lateral distributions of turbulent statistics on the lee side of steep hills with different height ratios. In general, it is found that the effects of the Coriolis force on the turbulent statistics are more significant in the central region ($y/L = 0$) than the surrounding regions. In addition, both the mean velocity and the turbulent kinetic energy are more sensitive to the Coriolis force as h/H increases. For steep hills with large height ratios ($h/H = 2/3, 1/3$), the higher mean wind speed and the lower turbulence energy are revealed at the position of $y/L = -0.5$ if the Coriolis force is neglected.

The speed-up factor ΔS at the hill crest is of vital importance for the assessment and utilization of wind power in mountainous areas. ΔS is defined as follows:

$$\Delta S = \frac{U(z') - U_0(z')}{U_0(z')} \tag{18}$$

where $U(z')$ is the mean velocity at the relative elevation z' above the local terrain ($z' = z - z_s$), and $U_0(z')$ is the reference mean velocity at the same elevation in the absence of the hill. Fig. 21 illustrates the vertical
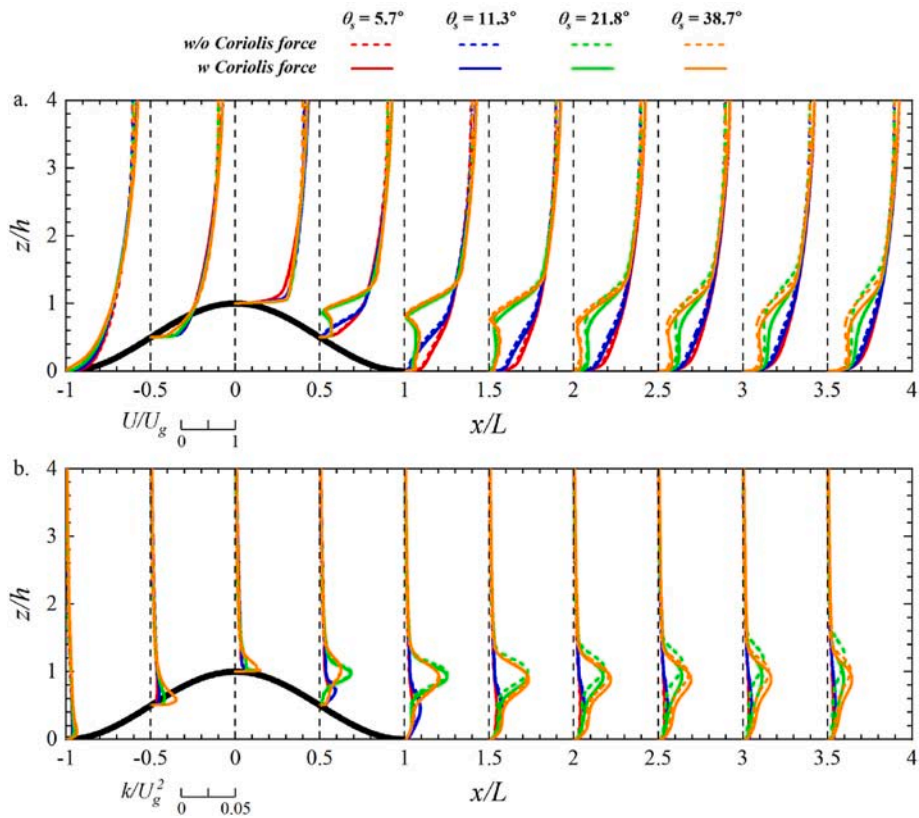
Fig. 17. Normalized profiles of turbulent statistics for atmospheric flows over three-dimensional hills with different hill slopes: (a) mean velocity and (b) turbulent kinetic energy at $y = 0$ plane.
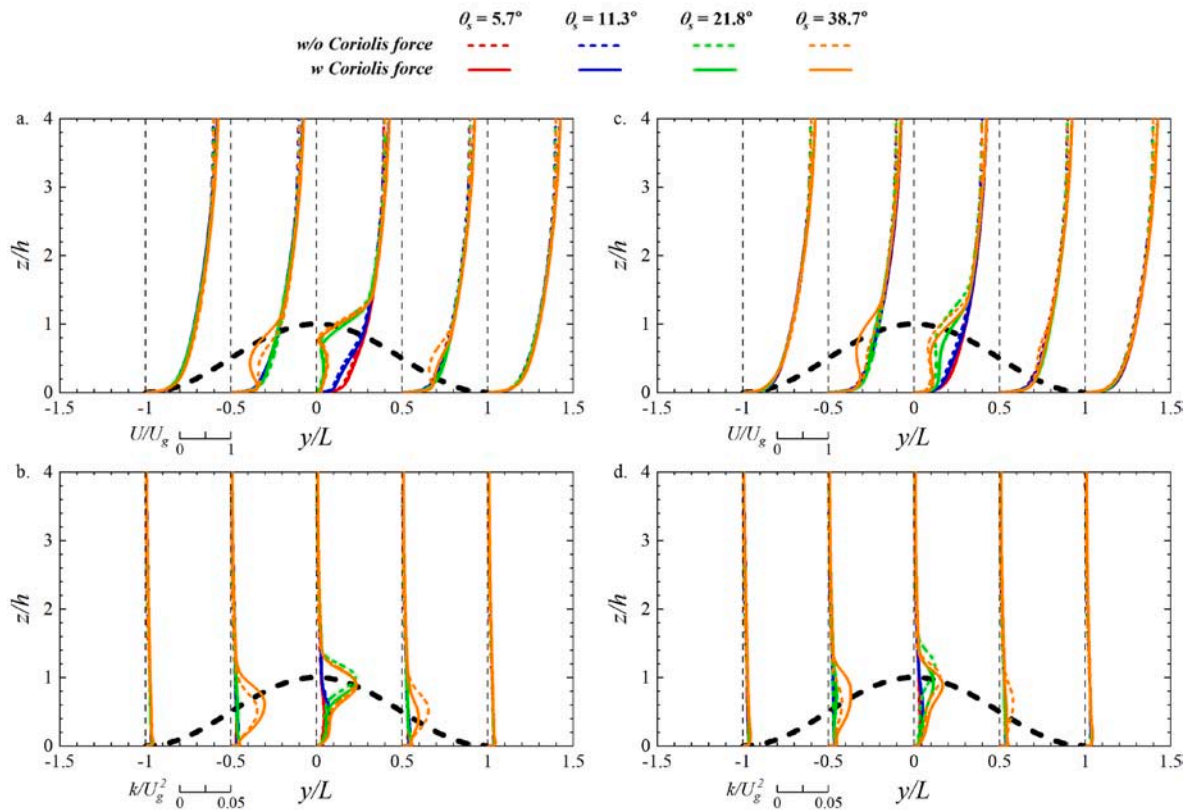

Fig. 18. Normalized profiles of turbulent statistics for atmospheric flows over three-dimensional hills with different hill slopes at several lateral planes: (a, b) $x = 1.5L$, (c, d) $x = 3L$.
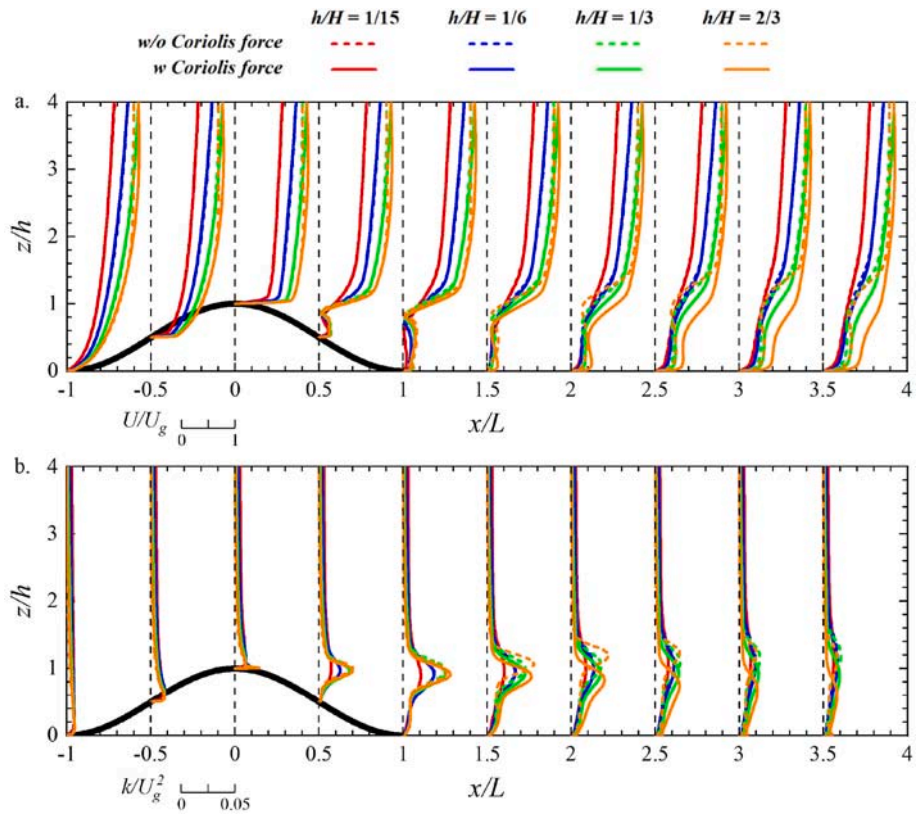
Fig. 19. Normalized profiles of turbulent statistics for atmospheric flows over three-dimensional hills with different height ratios: (a) mean velocity and (b) turbulent kinetic energy at $y = 0$ plane.
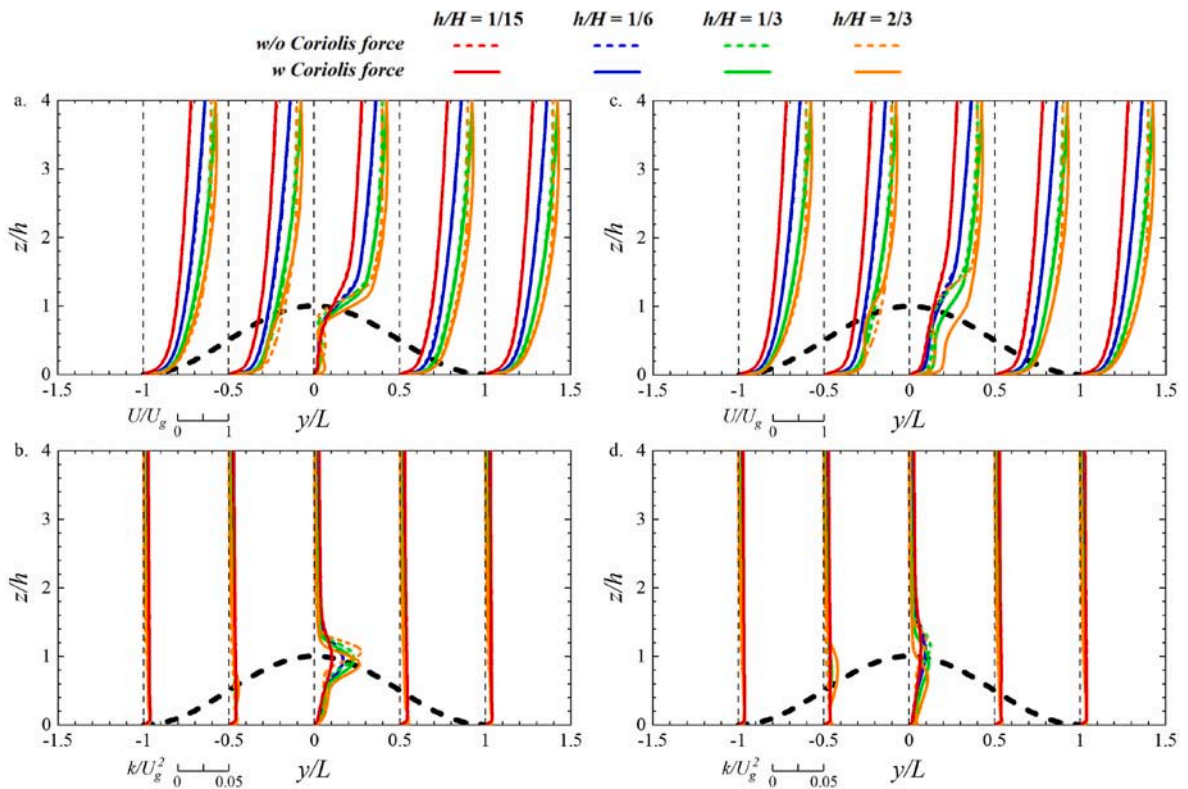

Fig. 20. Normalized profiles of turbulent statistics for the atmospheric flows over three-dimensional hills with different height ratios at several lateral planes: (a, b) $x = 1.5L$, (c, d) $x = 3L$.
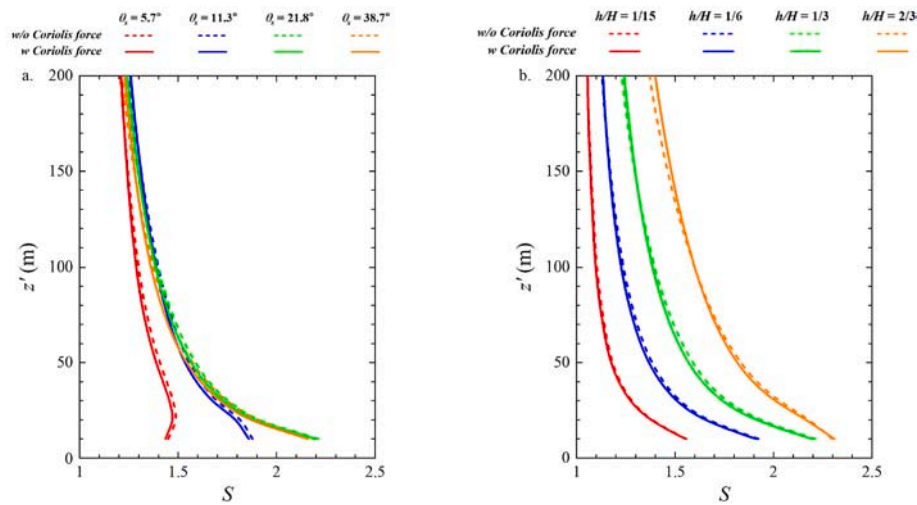
Fig. 21. Variations of the speed-up factor ΔS at the summit of three-dimensional hills with (a) different slopes and (b) height ratios.

variations of ΔS at the summit of three-dimensional hills with different slopes and height ratios. It is observed that ΔS at the hilltop is negligibly influenced by the Coriolis force, indicating that ΔS at the crest can be reasonably predicted by wind tunnel experiments that neglect the Coriolis effect. As the hill slope increases, the topographic speed-up effects above the top of 200 m high three-dimensional hills ($h/H = 1/3$) are considerably strengthened in the vicinity of the ground surface, whereas ΔS above the relative elevation z' of 150 m is slightly affected by slope of the hill ($\theta_s = 11.3°$, $21.8°$ and $38.7°$), as displayed in Fig. 21(a). Furthermore, it is revealed from Fig. 21(b) that ΔS at the crest of the three-dimensional steep hill ($\theta_s = 21.8°$) is substantially increased with increasing height ratios, which can be ascribed to the significant channel effects between the hill and the ABL.

6. Conclusions

In this study, numerical simulations are performed to systematically investigate atmospheric flows over flat terrain and three-dimensional hills considering the effects of Coriolis force. A new formula for l_{max} adopted in the LLS k-ε model is proposed based on LES simulations. The effects of Coriolis force on atmospheric flows over hills with different slopes and height ratios are clarified in terms of flow patterns and turbulent statistics. The major findings are summarized below:

1. The LLS k-ε model shows good performance in predicting the turbulent flow over a three-dimensional steep hill with rough surface. By setting an appropriate value of l_{max}, the LLS k-ε model can reasonably reproduce neutral engineering ABL flows over flat terrain considering the effects of Coriolis force.
2. A new formula for l_{max} is derived as a function of U_g, f_c and z_0 (surface Rossby number, $Ro_s = U_g/f_c z_0$), which can reasonably characterize the influence of different terrain roughness on neutral engineering ABL flows. Based on the proposed formula, the mean wind profiles for neutral ABL flows over flat terrain with different surface roughness can be predicted by the LLS k-ε model.
3. Wake deflection is identified on the lee side of three-dimensional hills owing to the vertical wind veer associated with the Coriolis force. As the hill slope and the height ratio increase, the velocity deficit in the hill wake recovers faster in the cases with the Coriolis force. However, the effects of Coriolis force on the speed-up factor at the hilltop is almost negligible, regardless of hill slopes and height ratios.

The outcome of this research work is of theoretical significance and practical value. First, the proposed formula for l_{max} can reveal the characteristics of mean wind profiles in neutral ABL flows over different terrain exposures whilst considering the effects of Coriolis force, which can further serve as a valuable reference for the development of inflow models in the wind energy industry. Secondly, the systematic investigation of the Coriolis effects on atmospheric flows over single isolated three-dimensional hills is expected to improve the understanding of turbulence characteristics over topography, which will be conducive to the layout optimization of wind farms in mountainous regions. However, it should be noted that the validity of the proposed l_{max} model needs further investigation in real large-scale complex terrain with steeper slopes. Finally, the effects of atmospheric thermal stratifications on turbulent flows over hills have not been considered in the present study and will be clarified in the future work.

CRediT authorship contribution statement

Tong Zhou: Methodology, Investigation, Formal analysis, Software, Validation, Visualization, Data curation, Writing – original draft. **Takeshi Ishihara:** Conceptualization, Methodology, Formal analysis, Funding acquisition, Project administration, Resources, Supervision, Writing – review & editing.

Declaration of competing interest

The authors declare that they have no known competing financial interests or personal relationships that could have appeared to influence the work reported in this paper.

Data availability

The authors do not have permission to share data.

References

AIJ-RLB-2015, 2015. Recommendations for Loads on Buildings. Architecture Institute of Japan, Tokyo, Japan.

Apsley, D.D., Castro, I.P., 1997. A limited-length-scale k-ε model for the neutral and stably-stratified atmospheric boundary layer. Boundary-Layer Meteorol. 83 (1), 75–98.

ASCE7-16, 2016. Minimum Design Loads for Buildings and Other Structures. American Society of Civil Engineers, Reston, the United States.

Berthaut-Gerentes, J., Delaunay, D., 2015. LES: unsteady atmospheric turbulent layer inlet. A precursor method application and its quality check. Computation 3 (2), 262–273.

Blackadar, A.K., 1962. The vertical distribution of wind and turbulent exchange in a neutral atmosphere. J. Geophys. Res. 67 (8), 3095–3102.

Brown, A.R., Hobson, J.M., Wood, N., 2001. Large-eddy simulation of neutral turbulent flow over rough sinusoidal ridges. Boundary-Layer Meteorol. 98 (3), 411–441.

Brown, A.R., Beljaars Ac, M., Hersbach, H., Hollingsworth, A., Miller, M., Vasiljevic, D., 2005. Wind turning across the marine atmospheric boundary layer. Q. J. R. Meteorol. Soc. 131, 1233–1250.

Caldwell, D.R., Van Atta, C.W., Helland, K.N., 1972. A laboratory study of the turbulent Ekman layer. Geophys. Fluid Dynam. 3 (2), 125–160.

Cao, S., Tamura, T., 2006. Experimental study on roughness effects on turbulent boundary layer flow over a two-dimensional steep hill. J. Wind Eng. Ind. Aerod. 94 (1), 1–19.

Cao, S., Tamura, T., 2007. Effects of roughness blocks on atmospheric boundary layer flow over a two-dimensional low hill with/without sudden roughness change. J. Wind Eng. Ind. Aerod. 95 (8), 679–695.

Cao, S., Wang, T., Ge, Y., Tamura, Y., 2012. Numerical study on turbulent boundary layers over two-dimensional hills—effects of surface roughness and slope. J. Wind Eng. Ind. Aerod. 104, 342–349.

Castorrini, A., Gentile, S., Geraldi, E., Bonfiglioli, A., 2021. Increasing spatial resolution of wind resource prediction using NWP and RANS simulation. J. Wind Eng. Ind. Aerod. 210, 104499.

Coleman, G.N., 1999. Similarity statistics from a direct numerical simulation of the neutrally stratified planetary boundary layer. J. Atmos. Sci. 56 (6), 891–900.

Conan, B., Chaudhari, A., Aubrun, S., van Beeck, J., Hämäläinen, J., Hellsten, A., 2016. Experimental and numerical modelling of flow over complex terrain: the Bolund hill. Boundary-Layer Meteorol. 158, 183–208.

Crawford, K.C., Hudson, H.R., 1973. The diurnal wind variation in the lowest 1500 ft in central Oklahoma. June 1966–May 1967. J. Appl. Meteorol. 12 (1), 127–132.

Deardorff, J.W., 1973. The use of subgrid transport equations in a three-dimensional model of atmospheric turbulence. J. Fluid Eng. 90, 429–438.

Detering, H.W., Etling, D., 1985. Application of the E-ε turbulence model to the atmospheric boundary layer. Boundary-Layer Meteorol. 33, 113–133.

Esau, I., 2003. The Coriolis effect on coherent structures in planetary boundary layers. J. Turbul. 4 (1), N17.

Esau, I., 2004. Simulation of Ekman boundary layers by large eddy model with dynamic mixed subfilter closure. Environ. Fluid Mech. 4 (3), 273–303.

Feng, C., Gu, M., 2020. Numerical study on self-sustainable atmospheric boundary layer considering wind veering based on steady k-ε model. Wind Struct. 30 (1), 69–83.

Feng, C., Gu, M., Zheng, D., 2019. Numerical simulation of wind effects on super high-rise buildings considering wind veering with height based on CFD. J. Fluid Struct. 91, 102715.

Ferreira, A.D., Lopes, A.M.G., Viegas, D.X., Sousa, A.C.M., 1995. Experimental and numerical simulation of flow around two-dimensional hills. J. Wind Eng. Ind. Aerod. 54, 173–181.

Flay, R.G.J., 1996. A twisted flow wind tunnel for testing yacht sails. J. Wind Eng. Ind. Aerod. 63 (1), 171–182.

Gadde, S.N., Stevens, R.J., 2019. Effect of Coriolis force on a wind farm wake. In: J. Phys. Conference Series, vol. 1256. IOP Publishing, 012026, 1.

GB50009-2012, 2013. Load Code for the Design of Building Structures. China Architecture & Building Press, Beijing, China.

Han, Y., Stoellinger, M.K., 2020. RANS simulations of neutral atmospheric boundary layer flow over complex terrain with comparisons to field measurements. Wind Energy 23 (2), 91–119.

He, Y.C., Chan, P.W., Li, Q.S., 2013. Wind profiles of tropical cyclones as observed by Doppler wind profiler and anemometer. Wind Struct. 17 (4), 419–433.

He, Y.C., Chan, P.W., Li, Q.S., 2016. Observations of vertical wind profiles of tropical cyclones at coastal areas. J. Wind Eng. Ind. Aerod. 152, 1–14.

Hess, G.D., Garratt, J.R., 2002a. Evaluating models of the neutral, barotropic planetary boundary layer using integral measures: Part I. Overview. Boundary-Layer Meteorol. 104 (3), 333–358.

Hess, G.D., Garratt, J.R., 2002b. Evaluating models of the neutral, barotropic planetary boundary layer using integral measures: Part II. Modelling observed conditions. Boundary-Layer Meteorol. 104 (3), 359–369.

Howroyd, G.C., Slawson, P.R., 1975. The characteristics of a laboratory produced turbulent Ekman layer. Boundary-Layer Meteorol. 8 (2), 201–219.

Ishihara, T., Fujino, Y., Hibi, K., 2001. A wind tunnel study of separated flow over a two-dimensional ridge and a circular hill. J. Wind Eng. 89, 573–576.

Ishihara, T., Hibi, K., 2002. Numerical study of turbulent wake flow behind a three-dimensional steep hill. Wind Struct. 5 (2–4), 317–328.

Ishihara, T., Hibi, K., Oikawa, S., 1999. A wind tunnel study of turbulent flow over a three-dimensional steep hill. J. Wind Eng. Ind. Aerod. 83 (1–3), 95–107.

Ishihara, T., Qi, Y., 2019. Numerical study of turbulent flow fields over steep terrain by using modified delayed detached-eddy simulations. Boundary-Layer Meteorol. 170 (1), 45–68.

Jiang, Q., Wang, S., Sullivan, P., 2018. Large-eddy simulation study of log laws in a neutral Ekman boundary layer. J. Atmos. Sci. 75 (6), 1873–1889.

Kamada, Y., Maeda, T., Yamada, K., 2019. Wind tunnel experimental investigation of flow field around two-dimensional single hill models. Renew. Energy 136, 1107–1118.

Kelly, M., van der Laan, M.P., 2023. From Shear to Veer: Theory, Statistics, and Practical Application. Wind Energy Sci. Discuss, pp. 1–37.

Kim, H.G., Lee, C.M., Lim, H.C., Kyong, N.H., 1997. An experimental and numerical study on the flow over two-dimensional hills. J. Wind Eng. Ind. Aerod. 66 (1), 17–33.

Koblitz, T., Bechmann, A., Sogachev, A., Sørensen, N., Réthoré, P.E., 2015. Computational Fluid Dynamics model of stratified atmospheric boundary-layer flow. Wind Energy 18 (1), 75–89.

Kosović, B., Curry, J.A., 2000. A large eddy simulation study of a quasi-steady, stably stratified atmospheric boundary layer. J. Atmos. Sci. 57 (8), 1052–1068.

Lettau, H., 1950. A re-examination of the "Leipzig wind profile" considering some relations between wind and turbulence in the frictional layer. Tellus 2 (2), 125–129.

Li, Q., Maeda, T., Kamada, Y., Yamada, K., 2017. Experimental investigation of flow over two-dimensional multiple hill models. Sci. Total Environ. 609, 1075–1084.

Lindvall, J., Svensson, G., 2019. Wind turning in the atmospheric boundary layer over land. Q. J. R. Meteorol. Soc. 145 (724), 3074–3088.

Liu, L., Stevens, R.J., 2021. Effects of atmospheric stability on the performance of a wind turbine located behind a three-dimensional hill. Renew. Energy 175, 926–935.

Liu, L., Stevens, R.J., 2022. Vertical structure of conventionally neutral atmospheric boundary layers. Proc. Natl. Acad. Sci. USA 119 (22), e2119369119.

Liu, Z., Diao, Z., Ishihara, T., 2019a. Study of the flow fields over simplified topographies with different roughness conditions using large eddy simulations. Renew. Energy 136, 968–992.

Liu, Z., Ishihara, T., He, X., Niu, H., 2016a. LES study on the turbulent flow fields over complex terrain covered by vegetation canopy. J. Wind Eng. Ind. Aerod. 155, 60–73.

Liu, Z., Ishihara, T., Tanaka, T., He, X., 2016b. LES study of turbulent flow fields over a smooth 3-D hill and a smooth 2-D ridge. J. Wind Eng. Ind. Aerod. 153, 1–12.

Liu, Z., Wang, W., Wang, Y., Ishihara, T., 2020. Large eddy simulations of slope effects on flow fields over isolated hills and ridges. J. Wind Eng. Ind. Aerod. 201, 104178.

Liu, Z., Zheng, C., Wu, Y., Flay, R.G.J., Zhang, K., 2019b. Investigation on the effects of twisted wind flow on the wind loads on a square section megatall building. J. Wind Eng. Ind. Aerod. 191, 127–142.

Liu, Z., Zheng, C., Wu, Y., Flay, R.G.J., Zhang, K., 2019c. Wind tunnel simulation of wind flows with the characteristics of thousand-meter high ABL. Build. Environ. 152, 74–86.

Lu, B., Li, Q.S., 2022. Large eddy simulation of the atmospheric boundary layer to investigate the Coriolis effect on wind and turbulence characteristics over different terrains. J. Wind Eng. Ind. Aerod. 220, 104845.

Mendenhall, B.R., 1967. A Statistical Study of Frictional Wind Veering in the Planetary Boundary Layer. Atmospheric Science Paper. No. 116.

Meng, Y., Matsui, M., Hibi, K., 1995. Characteristics of the vertical wind profile in neutrally atmospheric boundary layers Part 1: strong winds during non-typhoon climates. J. Wind Eng. 65, 1–15 (in Japanese).

Moeng, C.-H., 1984. A large-eddy-simulation model for the study of planetary boundary-layer turbulence. J. Atmos. Sci. 41, 2052–2062.

Pedersen, J.G., Gryning, S.E., Kelly, M., 2014. On the structure and adjustment of inversion-capped neutral atmospheric boundary-layer flows: large-eddy simulation study. Boundary-Layer Meteorol. 153 (1), 43–62.

Peña, A., Gryning, S.E., Floors, R., 2014. The turning of the wind in the atmospheric boundary layer. In: J. Phys. Conference Series, vol. 524. IOP Publishing, 012118, 1.

Peng, M.S., Li, S.W., Chang, S.W., Williams, R.T., 1995. Flow over mountains: Coriolis force, transient troughs and three dimensionality. Q. J. R. Meteorol. Soc. 121 (523), 593–613.

Petersen, G.N., Kristjánsson, J.E., Ólafsson, H., 2005. The effect of upstream wind direction on atmospheric flow in the vicinity of a large mountain. Q. J. R. Meteorol. Soc. 131 (607), 1113–1128.

Qian, G.W., Ishihara, T., 2022. A new wind turbine wake model considering the effect of Coriolis force. Proc. of Grand Renewable Energy 25. https://doi.org/10.24752/gre.2.0_25.

Qian, G.W., Song, Y.P., Ishihara, T., 2022. A control-oriented large eddy simulation of wind turbine wake considering effects of Coriolis force and time-varying wind conditions. Energy 239, 121876.

Richards, P.J., Hoxey, R.P., 1993. Appropriate boundary conditions for computational wind engineering models using the k-ε turbulence model. J. Wind Eng. Ind. Aerod. 46, 145–153.

Safaei Pirooz, A.A., Flay, R.G., 2018. Comparison of speed-up over hills derived from wind-tunnel experiments, wind-loading standards, and numerical modelling. Boundary-Layer Meteorol. 168 (2), 213–246.

Shu, Z.R., Li, Q.S., He, Y.C., Chan, P.W., 2020. Investigation of marine wind veer characteristics using wind lidar measurements. Atmosphere 11, 1178.

Shu, Z.R., Li, Q.S., He, Y.C., Chan, P.W., 2018. Observational study of veering wind by Doppler wind profiler and surface weather station. J. Wind Eng. Ind. Aerod. 178, 18–25.

Takahashi, T., Kato, S., Murakami, S., Ooka, R., Yassin, M.F., Kono, R., 2005. Wind tunnel tests of effects of atmospheric stability on turbulent flow over a three-dimensional hill. J. Wind Eng. Ind. Aerod. 93 (2), 155–169.

Tamura, T., Cao, S., Okuno, A., 2007a. LES study of turbulent boundary layer over a smooth and a rough 2D hill model. Flow, Turbul. Combust. 79 (4), 405–432.

Tamura, T., Okuno, A., Sugio, Y., 2007b. LES analysis of turbulent boundary layer over 3D steep hill covered with vegetation. J. Wind Eng. Ind. Aerod. 95 (9–11), 1463–1475.

Tse, K.T., Weerasuriya, A.U., Kwok, K.C.S., 2016. Simulation of twisted wind flows in a boundary layer wind tunnel for pedestrian-level wind tunnel tests. J. Wind Eng. Ind. Aerod. 159, 99–109.

van der Laan, M.P., Kelly, M., Floors, R., Peña, A., 2020. Rossby number similarity of an atmospheric RANS model using limited-length-scale turbulence closures extended to unstable stratification. Wind Ener. Sci. 5, 355–374.

Weerasuriya, A.U., Hu, Z.Z., Li, S.W., Tse, K.T., 2016. Wind direction field under the influence of topography, part I: a descriptive model. Wind Struct. 22 (4), 455–476.

Weerasuriya, A.U., Tse, K.T., Zhang, X., Li, S.W., 2018. A wind tunnel study of effects of twisted wind flows on the pedestrian-level wind field in an urban environment. Build. Environ. 128, 225–235.

Wyngaard, J.C., 2004. Toward numerical modeling in the "Terra Incognita". J. Atmos. Sci. 61 (14), 1816–1826.

Yang, Q., Zhou, T., Yan, B., Liu, M., Van Phuc, P., Shu, Z., 2021. LES study of topographical effects of simplified 3D hills with different slopes on ABL flows considering terrain exposure conditions. J. Wind Eng. Ind. Aerod. 210, 104513.

Yeo, D.H., Simiu, E., 2010. Database-assisted Design for Wind: Veering Effects on High-Rise Structures. Technical Note (NIST TN)-1672.

Yeo, D., 2012. Practical estimation of veering effects on high-rise structures: a database-assisted design approach. Wind Struct. 15 (5), 355–367.

Yoshizawa, A., Horiuti, K., 1985. A statistically-derived subgrid-scale kinetic energy model for the large-eddy simulation of turbulent flows. J. Phys. Soc. Jpn. 54 (8), 2834–2839.

Zhou, T., Yan, B., Yang, Q., Hu, W., Chen, F., 2022. POD analysis of spatiotemporal characteristics of wake turbulence over hilly terrain and their relationship to hill slope, hill shape and inflow turbulence. J. Wind Eng. Ind. Aerod. 224, 104986.